

Piecewise Potential Vorticity Inversion

By

Chanh Q. Kieu

A scholarly paper in partial fulfillment of the requirements for the degree of

Master of Science

October 2005

Department of Atmospheric and Oceanic Science

University of Maryland, College Park

Maryland

Advisor: Prof. Da-Lin Zhang

Table of Contents

| | Page |
|---|------|
| Abstract..... | 2 |
| Acknowledgement | 3 |
| PART I. Theoretical Development | 4 |
| Chapter 1. Introduction..... | 4 |
| Chapter 2. Formulation of PV system..... | 10 |
| Chapter 3. Boundary condition..... | 18 |
| Chapter 4. Approaches toward the calculations of the mean fields..... | 22 |
| Chapter 5. New methodology of calculation..... | 25 |
| PART II. Application to Hurricane Bonnie | 27 |
| Chapter 6. Overview of Hurricane Bonnie | 27 |
| Chapter 7. Piecewise PV inversion..... | 31 |
| Chapter 8. Summary and conclusions..... | 38 |
| Appendix | 40 |
| References..... | 42 |
| Figure Captions..... | 46 |
| Figures..... | 47 |

Abstract

In this work, we first extend the Potential Vorticity (PV) inversion technique developed in Wang and Zhang (2003), which has proven to be of practical applications in hurricane studies and obtained some remarkable results, from the case of one PV piece to the case of an arbitrarily large number of PV pieces. Second, a new algorithm for solving piecewise PV inversion with any number of pieces will be proposed, which does not require solving simultaneously $2N$ nonlinear equations as proposed in previous works. Former approaches to piecewise PV inversion have a key obstacle: the number of equations needed to be solved increases as twice as the number of PV pieces. This makes iteration method become very sensitive to model parameters and to each specific application. Our new approach overcomes particularly this difficulty. In addition, the boundary condition problem for piecewise PV inversion will be investigated in more detailed. We also present an alternative way to calculate the mean balanced fields so that the application of piecewise PV inversion will be more practical and more wide-ranging. These above improvements will then be applied to Hurricane Bonnie 1998 to study diagnostically the mechanisms responsible for eyewall replacement processes. Previous studies as well as observations have recorded sometimes a stage of double eyewall in hurricane development but there appears to have no specific answer about the mechanisms for this process to date. Using the newly developed piecewise PV system, we have obtained some remarkable results that offer new insights into the processes leading to the replacement of hurricane eyes. Results obtained show evidently the high applicability of our improvements, which allow piecewise PV inversion to have broader applications.

Acknowledgment

I am deeply indebted to Prof. Dalin Zhang for his endless inspirations and enthusiasms in helping and supporting my researches. I also would like to thank Dr. Xingbao Wang and Dr. Tong Zhu for their assistants in data and providing me PV codes. Last but not least, I am very grateful to the Vietnam Educational Foundation for their supporting me during this research.

PART I. THEORETICAL DEVELOPMENT

Chapter 1. Introduction

Balanced flow is an important concept in understanding the atmospheric dynamics. At the meso- or smaller scales, meteorological flows are often dominated by many stochastic motions, leading to the development of unbalanced flows. However the unbalanced flows will quickly adjust to a balanced state through the so-called adjustment process (Holton 1993; Gill 1982). The adjustment processes often accompany many different kinds of waves such as gravity waves or inertial-gravity waves, and the time scale for such adjustments depends very much on the scale of motion, ranging from a few hours to several days. An important question is: given a meteorological system, such as an upper-level trough, a supercell storm, or a hurricane, to what spatial and temporal extents will this system influence the large scale flows at the later time? Answering such a question requires the knowledge of *the balanced flows rather than the instantaneous flows* because it is the balanced flows that persist long enough and contribute the most after adjustment processes. As an example, consider the case of an upper –level trough migrating into some area. The upper-level trough usually induces a process called cyclogenesis at the surface, and it is the balanced flows associated with this trough that are able to penetrate deeply to the surface. Another example is the question of how much a hurricane can influence the track and intensity of another hurricane nearby. In all of these cases, balanced flows play an important role.

Several approaches could be used to obtain balanced flows. Krishnamurti (1968) presented a system of balance equations which can be used to find the balanced flows for the

cases of large Rossby number. Nevertheless, this approach conceals the conservative characteristics of the system, and it does not allow for investigating the balanced flows associated with a specific weather pattern inside the domain. The second approach is based on the concept of potential vorticity (PV) Inversion. The striking feature of PV has long been recognized since its first introduction by Rossby in 1947. Emerging first as a good tracer of air mass, it was then quickly realized that PV is a very powerful and succinct dynamical quantity. A more comprehensive review of the historical development of PV can be found in Hoskin et. al. (1985). There are two important properties of PV concept which allow for an understanding of the three-dimensional (3D) balanced dynamics: the conservation of PV in the absence of frictional and diabatic processes, and the invertibility principle. Given a PV distribution and appropriate boundary conditions, it is possible to obtain the 3D balanced dynamical fields by using the invertibility principle. The balanced flows obtained from the PV system consist of geopotential height and streamfunction. From these two balanced flows, all the other variables, such as wind, temperature, and pressure fields, will follow immediately.

The PV inversion is usually categorized into two different forms: one is referred to as quasi-geostrophic PV (QG PV) inversion, and the other is isentropic PV inversion (IPV¹). For the case of QG PV, the geostrophic relationship between the wind and mass fields will be employed. This approximation results in a linear system for PV inversion, which makes QG PV inversion simple and easy to perform. The disadvantage of QG PV is the inaccuracy as the Rossby number becomes large, or flows are baroclinic. In the case of fully baroclinic and

¹ IPV is also sometimes mentioned as Ertel PV or Rossby PV. Usually, Ertel PV is reserved for the vertical projection of IPV.

compressible flow, it is necessary to take into account the 3D absolute vorticity vector which forms the essence of IPV.

Before the work of Hoskin et al. (1985), most of the applications of PV inversion were confined to QG PV inversion. It had to wait until the detailed works of Davis and Emanuel (1991, hereafter referred to as DE91) and Davis (1992) about the piecewise PV inversion does the application of PV inversion receive more attention, especially at the mesoscale. The philosophy of piecewise inversion is to separate the total PV distribution q into a mean field \bar{q} and an anomaly field q' . The PV anomaly q' will then be partitioned into N smaller PV pieces q'_i . The way we partition the total PV anomaly q' into smaller pieces depends on each specific application. For example, one may want to investigate the balanced impacts of the upper-level PV on the surface flows. In this case, one can divide the total PV anomaly q' into two parts: one at the upper level q'_u and the other is the remaining q'_r , and perform a PV inversion for the upper PV piece q'_u . From the requirement that the mean fields² satisfy a nonlinear balance equation, we will obtain a system of equations for perturbations and it is possible to calculate the 3D balanced perturbations associated with any PV piece. The method proposed by DE91 guarantees that the sum of all balanced perturbation fields obtained by inverting each PV piece q'_i will be equal to the inversion of the total PV anomaly q' . Piecewise PV inversion allows one to study the impact of any PV piece in a balanced way.

Because of the high applicability of DE91's work, piecewise PV inversion has been employed extensively in many studies to investigate the 3D balanced fields of mesoscale systems since then. For example, Wu and Emanuel (1995a, b), Shapiro and Franklin (1995)

² The mean fields (or perturbation fields) mentioned in this work are the fields associated with the PV system, which consists of streamfunction, geopotential height, and potential vorticity

applied the piecewise PV inversion technique to investigate the impact of environment PV anomalies on hurricane movement. Using the same piecewise PV technique, Zhang et. al. (2002), have shown some significant influences of upper-level PV anomalies on multiple frontal cyclogenesis. In another fashion, Huo et. al. (1997, 1999) used the piecewise PV inversion to improve the initial condition for the prediction of a superstorm. Another example is the work of Shapiro and Möller (2002) in which they used the piecewise PV inversion to examine the influence of asymmetrical flows on the intensification of hurricane Opal.

So far, the most disturbing issue of the current piecewise PV inversion technique is: when there are N PV pieces ($N > 1$), it is required to iterate simultaneously $2N$ nonlinear partial differential equations (the details for the inversion of N pieces can be found, e.g. in Shapiro 1996). If the number of PV pieces and the number of grid points are large enough, this iteration method will become unstable, time consuming, and not practical. In addition, the convergence of iteration for $2N$ nonlinear equations is challenging, and it appears to be unrealistic to follow DE91's scheme when there are more than three PV pieces. This limitation of piecewise PV inversion is the reason why many applications of PV inversion technique have so far confined only to one piece rather than N pieces as theoretically developed. Recently, Wang and Zhang (2003, hereafter referred to as WZ03) have developed a PV inversion technique applied to hurricanes and obtained some significant results. The technique developed in ZW03 has an advantage of introducing a new parameter ϵ , which can be adjusted to control the convergence of PV system, and shows some improvements in examining hurricane dynamics. However, WZ03's development is again applicable to the case of one PV piece only.

Thus, the objectives of the present scholarly paper will be to:

- i) Extend the PV inversion developed in WZ03 from *one PV piece to N PV pieces*;
- ii) Develop a new algorithm for solving the N-piecewise PV system so that the application of the piecewise technique will be more practical; and
- iii) Address the problem of partitioning the total fields into mean and anomaly in detail.

There are two motivating scientific questions that can be approached from point of view of piecewise PV inversion:

1. What are the mechanisms responsible for eyewall replacement process captured from both observations and numerical simulations?
2. Why the PV at the core of a hurricane keeps following closely the general development of a hurricane in the absence of any source of heating?

The main purpose in this work is to tackle the first question to provide more understandings to eyewall replacement processes. The newly developed PV inversion scheme will be applied to Hurricane Bonnie (1998) for this purpose. During the August 26 1998, Bonnie showed a stage of double eyewalls with the eyewall replacement process occurring quite evidently, and it is therefore a good case to investigate. By applying the piecewise PV inversion technique developed herein, we obtain some remarkable results that address specifically the processes leading to the replacement of Bonnie's eyewall.

A more careful scrutiny of previous studies (e.g. DE91; Shapiro 1996; Morgan 1999; WZ03) indicates that little has been discussed about the uniqueness and the existence of the solution for the system of equations associated with piecewise PV inversion (with the combined Newman and Dirichle boundary conditions). Although there are some experimental indications about the criteria for the convergence (e.g., $PV > 0$ in DE91), a mathematical proof for the existence and uniqueness does not exist. Note that it is not

possible to categorize the system of equations for piecewise PV inversion into elliptic, hyperbolic, or parabolic types as usual because this is a system of nonlinear equations, *not a single linear partial differential equation*. It turns out that the questions of uniqueness and existence are virtually impossible to answer analytically and will be neglected here. For hereafter applications, it will be assumed that solutions will always exist and be unique.

Chapter 2. Formulation

It is necessary first to derive the nonlinear balance (NLB) equation. Starting with the divergent equation in the pressure coordinate:

$$\frac{dD}{dt} + \left[\left(\frac{\partial u}{\partial x} \right)^2 + 2 \frac{\partial v}{\partial x} \frac{\partial u}{\partial y} + \left(\frac{\partial v}{\partial y} \right)^2 \right] + \left[\frac{\partial \omega}{\partial x} \frac{\partial u}{\partial p} + \frac{\partial \omega}{\partial y} \frac{\partial v}{\partial p} \right] = -\nabla^2 \Phi + f\zeta + v \frac{\partial f}{\partial y} - u \frac{\partial f}{\partial x} + \nabla_h \cdot F_r \quad (2.1)$$

where $D = \frac{\partial u}{\partial x} + \frac{\partial v}{\partial y}$ is divergence, $\zeta = \frac{\partial v}{\partial x} - \frac{\partial u}{\partial y}$ is the relative vorticity in the vertical direction, f is the Coriolis parameter, F_r is friction, and ∇_h is the horizontal divergent operator. After making some scaling evaluations (Holton 1993), Eq. (2.1) becomes:

$$\left(\frac{\partial u}{\partial x} \right)^2 + 2 \frac{\partial v}{\partial x} \frac{\partial u}{\partial y} + \left(\frac{\partial v}{\partial y} \right)^2 = -\nabla^2 \Phi + f\zeta + v \frac{\partial f}{\partial y} - u \frac{\partial f}{\partial x} + \nabla_h \cdot F_r \quad (2.2)$$

Using the Helmholtz theorem, the horizontal wind field \mathbf{V}_h is decomposed into the rotational and divergent components:

$$\mathbf{V}_h = (u, v) = \mathbf{V}_\psi + \mathbf{V}_\chi = -\nabla \Psi \times \mathbf{k} + \nabla \chi \quad (2.3)$$

Substituting Eq. (2.3) into Eq. (2.2) and restricting the resulting equation to the order of $O(\mathbf{R}_\psi)$, where $\mathbf{R}_\psi \equiv \mathbf{V}_\psi / Lf_0$ is defined as the Rossby number for rotational wind, gives the NLB equation:

$$\nabla^2 \Phi = \nabla_h \cdot (f \nabla_h \Psi) + 2J \left(\frac{\partial \Psi}{\partial x}, \frac{\partial \Psi}{\partial y} \right) + \nabla_h \cdot F_r \quad (2.4)$$

where J is Jacobian operator. In deriving NLB equation (2.4), terms of order $O(\mathbf{V}_\chi/Lf_0)$ have been neglected³. It should be emphasized that this scaling approximation is applied only to the divergent equation (2.2), and this neglect does not mean that \mathbf{V}_χ is completely ignored. It turns out that the quasi-balanced divergent wind component \mathbf{V}_χ will be recovered in the omega equation (DE91; Wang and Zhang 2003, see the appendix for the system of omega equations)

To close the system for two unknowns ψ and ϕ , it is required to have one more equation relating ψ and ϕ . A careful inspection will show that the hydrostatic equation is a good candidate for our purpose. This hydrostatic equation connects geopotential with potential temperature by the following relationship:

$$\theta = \frac{\partial \Phi}{\partial \pi} \quad (2.5)$$

where π is the Exner function ($\pi=C_p(p/p_0)^\kappa$, $\kappa= R_d/C_p$). Given a potential temperature distribution, one can easily obtain the balanced geopotential height ϕ by directly integrating the hydrostatic equation (2.5). Using equation (2.4), the balanced streamfunction ψ will follow immediately. *However, the information from the potential temperature alone does not contain any dynamical properties of the system.* Moreover, this simple approach does not allow one to have a knowledge of the balanced impacts related to some particular systems such as upper-level troughs, mesoscale convective systems, or hurricanes. Here, PV becomes an important dynamical variable to address the above issues. The definition of IPV is given as

$$Q = \frac{1}{\rho} \boldsymbol{\eta} \cdot \nabla \theta_p \quad (2.6)$$

³ \mathbf{V}_χ is mentioned as the Rossby number for divergent wind (see DE91)

where ρ is the density of air, $\eta = 2\mathbf{\Omega} + \nabla \times \mathbf{V}$ is the absolute vorticity vector, and θ_p is the potential temperature. *The information contained in this PV quantity is not only potential temperature but also absolute vorticity and the stratification of the atmosphere.* Using the hydrostatic equation to replace the potential temperature in Eq. (2.6) by geopotential, and decomposing the wind field into the rotational and divergent components, equation (2.6) can be rewritten in a different form as follows:

$$Q = \frac{1}{r(z)} \frac{\theta_0}{G} \left[(f + \nabla_h^2 \Psi) \frac{\partial^2 \Phi}{\partial z^2} - \frac{\partial^2 \Psi}{\partial x \partial z} \frac{\partial^2 \Phi}{\partial x \partial z} - \frac{\partial^2 \Psi}{\partial y \partial z} \frac{\partial^2 \Phi}{\partial y \partial z} \right] \quad (2.7)$$

where $z = [1 - (P/P_0)^{R/C_p}](C_p \theta_0 / g)$ is the vertical pseudo-height coordinate, G is gravitational constant, and $r(z) = \rho_0 (P/P_0)^{R/C_p}$ is pseudodensity. Note that vertical velocity has been neglected when we go from (2.6) to (2.7). Also in deriving this equation, the disappearance of the χ -component of wind is due to the curl operator ($\nabla \times \nabla \chi = 0$), not because of the nondivergent approximation as in deriving the balance equation (2.4).

Eqs. (2.4) and (2.7) form a close system for ψ and ϕ . That is, given a distribution of PV and appropriate boundary conditions, Eqs. (2.4) and (2.7) could be iterated simultaneously to find ψ and ϕ . It is clear that computing the balanced flows from the system of Eqs. (2.4) and (2.7) is much more complicated than from the system of Eqs. (2.4) and (2.5), whilst both systems give the same 3D balanced dynamics. So, what is the role of PV here? As we shall see later, the main advantage of PV concept will be apparent when piecewise PV inversion is introduced. It turns out that PV can be used to classify quantities of different meteorological origins, such as upper-level troughs, environmental PV anomalies. Using piecewise PV inversion, it is possible to study the impacts of these different PV anomalies in a balanced way.

In practice, one is often more interested in examining the PV anomaly rather than investigating the whole PV distribution. This is because it is the PV anomaly that is closely associated with weather patterns. Therefore, it is essential to develop an efficient way to separate the total PV into mean and perturbation fields. In this work, the method developed by DE91 will be employed for which the total PV field is partitioned into a mean field and a perturbation field as follows: $Q = \bar{Q} + Q'$, $\Psi = \bar{\Psi} + \Psi'$, and $\Phi = \bar{\Phi} + \Phi'$. The mean fields: \bar{Q} , $\bar{\Psi}$ and $\bar{\Phi}$ are not taken arbitrarily, but two mean fields out of three must be obtained by inverting equations (2.4) and (2.7) given the remaining. With the total and mean PV field available in hand, the total PV anomaly Q' can follow easily, and our next task is to perform an inversion to find the perturbation streamfunction ψ' and geopotential ϕ' .

As a matter of fact, the PV anomaly Q' is still too wide-ranging. Some particular weather patterns have a spatial scale much smaller than the domain under consideration. For example, hurricanes have an extent of 500 km while the model domain may cover an area as large as 3000 km. As a result, a large part of PV anomalies in the whole domain has little importance. One thus continues to partition the total PV anomaly Q' into smaller PV pieces Q'_i , and tries to find the balanced perturbation fields ψ'_k and ϕ'_k associated with one particular PV piece Q'_k , which contains some useful information.

Because of the nonlinearity of the system of equations (2.4) and (2.7), *the perturbation fields ψ'_i and ϕ'_i are not only determined by the PV piece Q'_i but also influenced by other PV pieces.* This means that given some PV piece Q'_k with all required boundary conditions, it is not enough to find ψ'_k and ϕ'_k associated with Q'_k by using the invertibility principle. Only in the case of one and only one PV piece ($N = 1$), it is possible to perform an inversion of piece Q'_k to find ψ'_k and ϕ'_k . In the case $N > 1$, we are confronted

with the problem of how to obtain the perturbation balanced fields ψ'_i and ϕ'_i related to PV piece Q'_i such that the sum of all perturbation fields ψ'_i and ϕ'_i will be equal to the inversion of total PV perturbation Q' , i.e., the following relations must hold:

$$\psi' = \sum_{i=1}^N \psi'_i \quad \text{and} \quad \phi' = \sum_{i=1}^N \phi'_i \quad \text{if} \quad Q' = \sum_{i=1}^N Q'_i$$

where ψ' and ϕ' are obtained by inverting the total PV anomaly Q' . It turns out that there are an infinite ways to partition as investigated partly by DE91 [see also Davis (1992) for more discussion]. Here, we will follow DE91's method. Given the total PV anomaly Q' , we now

partition this Q' into N pieces $Q' = \sum_{i=1}^N Q'_i$. The i -th perturbation fields ψ'_i and ϕ'_i associated

with piece Q'_i are then given by the following system:

$$\nabla^2 \Phi'_i = \nabla(f \nabla \Psi'_i) + 2 \left(\frac{\partial^2 \Psi^*}{\partial x^2} \frac{\partial^2 \Psi'_i}{\partial y^2} - 2 \frac{\partial^2 \Psi^*}{\partial x \partial y} \frac{\partial^2 \Psi'_i}{\partial x \partial y} + \frac{\partial^2 \Psi^*}{\partial y^2} \frac{\partial^2 \Psi'_i}{\partial x^2} \right) \quad (2.8)$$

$$Q'_i = (f + \nabla^2 \Psi^*) \frac{\partial^2 \Phi'_i}{\partial z^2} + \nabla^2 \Psi'_i \frac{\partial^2 \Phi^*}{\partial z^2} - \left(\frac{\partial^2 \Psi^*}{\partial x \partial z} \frac{\partial^2 \Phi'_i}{\partial x \partial z} - \frac{\partial^2 \Phi^*}{\partial x \partial z} \frac{\partial^2 \Psi'_i}{\partial x \partial z} \right) - \left(\frac{\partial^2 \Psi^*}{\partial y \partial z} \frac{\partial^2 \Phi'_i}{\partial y \partial z} - \frac{\partial^2 \Phi^*}{\partial y \partial z} \frac{\partial^2 \Psi'_i}{\partial y \partial z} \right) \quad (2.9)$$

where $(\phi, \psi)^* = (\bar{\phi}, \bar{\psi}) + \frac{1}{2} \sum_{i=1}^N (\phi'_i, \psi'_i)$. Recall that \bar{Q} , $\bar{\Psi}$ and $\bar{\Phi}$ in equations (2.8) and (2.9)

satisfy both equations (2.4) and (2.7). The price we have to pay for the requirement that the sum of the inversion of each PV piece Q'_i be equal to the inversion of total PV anomaly Q' is that all ψ'_j and ϕ'_j with $j \neq i$ must be known in advance in order to find ψ'_i and ϕ'_i . Because these perturbation fields ψ'_j and ϕ'_j are unknown, a system of $2N$ nonlinear equations in the form of equations (2.8) and (2.9) need to be solved simultaneously.

In their work, WZ03 have presented a method for one-piece PV inversion by combining (2.8) and (2.9) to obtain a new set of equations in which a new parameter ε is introduced. By allowing this free parameter to vary from 0 to 1, it is possible to control the convergence of the system effectively. Our purpose now is to extend this technique to a full piecewise inversion applied for the case with an arbitrary number of PV pieces ($N > 1$). Following WZ03, we multiply Eq. (2.8) by a parameter ε ($0 < \varepsilon < 1$), and add it into Eq. (2.9). Using the explicit expression for ψ^* and ϕ^* , after some manipulations, we get:

$$\begin{aligned}
& (\mathcal{E} + \frac{\partial^2 \bar{\Phi}}{\partial z^2}) \nabla^2 \Psi'_i = Q'_i - (f + \nabla^2 \bar{\Psi}) \frac{\partial^2 \Phi'_i}{\partial z^2} + \frac{\partial^2 \bar{\Psi}}{\partial x \partial z} \frac{\partial^2 \Phi'_i}{\partial x \partial z} + \frac{\partial^2 \bar{\Phi}}{\partial x \partial z} \frac{\partial^2 \Psi'_i}{\partial x \partial z} + \frac{\partial^2 \bar{\Psi}}{\partial y \partial z} \frac{\partial^2 \Phi'_i}{\partial y \partial z} + \frac{\partial^2 \bar{\Phi}}{\partial y \partial z} \frac{\partial^2 \Psi'_i}{\partial y \partial z} \\
& - \frac{1}{2} (\sum_{n=1} \nabla^2 \Psi'_n \frac{\partial^2 \Phi'_i}{\partial z^2} + \nabla^2 \Psi'_i \sum_{n=1} \frac{\partial^2 \Phi'_n}{\partial z^2}) + \frac{1}{2} (\sum_{n=1} \frac{\partial^2 \Psi'_n}{\partial x \partial z} \frac{\partial^2 \Phi'_i}{\partial x \partial z} + \sum_{n=1} \frac{\partial^2 \Phi'_n}{\partial x \partial z} \frac{\partial^2 \Psi'_i}{\partial x \partial z}) + \\
& + \frac{1}{2} (\sum_{n=1} \frac{\partial^2 \Psi'_n}{\partial y \partial z} \frac{\partial^2 \Phi'_i}{\partial y \partial z} + \sum_{n=1} \frac{\partial^2 \Phi'_n}{\partial y \partial z} \frac{\partial^2 \Psi'_i}{\partial y \partial z}) \\
& + \varepsilon [\nabla^2 \Phi'_i - \beta \frac{\partial \Psi'_i}{\partial y} - 2 (\frac{\partial^2 \bar{\Psi}}{\partial x^2} \frac{\partial^2 \Psi'_i}{\partial y^2} - 2 \frac{\partial^2 \bar{\Psi}}{\partial x \partial y} \frac{\partial^2 \Psi'_i}{\partial x \partial y} + \frac{\partial^2 \bar{\Psi}}{\partial y^2} \frac{\partial^2 \Psi'_i}{\partial x^2}) - (\sum_{n=1} \frac{\partial^2 \Psi'_n}{\partial x^2} \frac{\partial^2 \Psi'_i}{\partial y^2} - \\
& - 2 \sum_{n=1} \frac{\partial^2 \Psi'_n}{\partial x \partial y} \frac{\partial^2 \Psi'_i}{\partial x \partial y} + \sum_{n=1} \frac{\partial^2 \Psi'_n}{\partial y^2} \frac{\partial^2 \Psi'_i}{\partial x^2}) + \frac{\partial f_x}{\partial x} + \frac{\partial f_y}{\partial y}]
\end{aligned} \tag{2.10}$$

A second equation for ψ'_i and ϕ'_i can be obtained by subtracting Eq. (2.8) from (2.9) and rearranging:

$$\begin{aligned}
\nabla^2 \Phi'_i + (f + \nabla^2 \bar{\Psi}) \frac{\partial^2 \Phi'_i}{\partial z^2} &= Q'_i - \nabla^2 \Psi'_i \frac{\partial^2 \bar{\Phi}}{\partial z^2} + f \nabla^2 \Psi'_i + \beta \frac{\partial \Psi'_i}{\partial y} + \frac{\partial f_x}{\partial x} + \frac{\partial f_y}{\partial y} \\
-\frac{1}{2} \left(\sum_{n=1} \nabla^2 \Psi'_n \frac{\partial^2 \Phi'_i}{\partial z^2} + \nabla^2 \Psi'_i \sum_{n=1} \frac{\partial^2 \Phi'_n}{\partial z^2} \right) &+ \frac{\partial^2 \bar{\Psi}}{\partial x \partial z} \frac{\partial^2 \Phi'_i}{\partial x \partial z} + \frac{\partial^2 \bar{\Phi}}{\partial x \partial z} \frac{\partial^2 \Psi'_i}{\partial x \partial z} + \frac{\partial^2 \bar{\Psi}}{\partial y \partial z} \frac{\partial^2 \Phi'_i}{\partial y \partial z} + \frac{\partial^2 \bar{\Phi}}{\partial y \partial z} \frac{\partial^2 \Psi'_i}{\partial y \partial z} \\
+\frac{1}{2} \left(\sum_{n=1} \frac{\partial^2 \Psi'_n}{\partial x \partial z} \frac{\partial^2 \Phi'_i}{\partial x \partial z} + \sum_{n=1} \frac{\partial^2 \Phi'_n}{\partial x \partial z} \frac{\partial^2 \Psi'_i}{\partial x \partial z} \right) &+ \frac{1}{2} \left(\sum_{n=1} \frac{\partial^2 \Psi'_n}{\partial y \partial z} \frac{\partial^2 \Phi'_i}{\partial y \partial z} + \sum_{n=1} \frac{\partial^2 \Phi'_n}{\partial y \partial z} \frac{\partial^2 \Psi'_i}{\partial y \partial z} \right) + \\
+ 2 \left(\frac{\partial^2 \bar{\Psi}}{\partial x^2} \frac{\partial^2 \Psi'_i}{\partial y^2} - 2 \frac{\partial^2 \bar{\Psi}}{\partial x \partial y} \frac{\partial^2 \Psi'_i}{\partial x \partial y} + \frac{\partial^2 \bar{\Psi}}{\partial y^2} \frac{\partial^2 \Psi'_i}{\partial x^2} \right) & \\
+ 2 \left(\frac{1}{2} \sum_{n=1} \frac{\partial^2 \Psi'_n}{\partial x^2} \frac{\partial^2 \Psi'_i}{\partial y^2} - 2 \frac{1}{2} \sum_{n=1} \frac{\partial^2 \Psi'_n}{\partial x \partial y} \frac{\partial^2 \Psi'_i}{\partial x \partial y} + \frac{1}{2} \sum_{n=1} \frac{\partial^2 \Psi'_n}{\partial y^2} \frac{\partial^2 \Psi'_i}{\partial x^2} \right) &
\end{aligned} \tag{2.11}$$

Note that although the system of equations (2.10) and (2.11) are now applied for the case of N PV pieces, the elliptic condition for Eq. (2.10) is still the same as that for the case of one PV piece (using the same elliptic criteria of equation (2.10) as in WZ03) and is given by:

$$(\mathcal{E}f + 2\varepsilon \frac{\partial^2 \bar{\Psi}}{\partial x^2} + \frac{\partial^2 \bar{\Phi}}{\partial z^2}) (\mathcal{E}f + 2\varepsilon \frac{\partial^2 \bar{\Psi}}{\partial y^2} + \frac{\partial^2 \bar{\Phi}}{\partial z^2}) - 4\varepsilon^2 \left(\frac{\partial^2 \bar{\Psi}}{\partial x \partial y} \right)^2 > 0 \tag{2.12}$$

The advantage of this ε -multiplication is that the value of ε can now be varied appropriately so that the system of equations (2.11) and (2.12) will converge. As it is clear from (2.12), this ε parameter is expected to be small in order for the elliptic condition (2.12) to be satisfied. This is because the first product term on the LHS of (2.12) is proportional to ε and thus decreases slower than the last term, which is second order in ε , when ε approaches to zero. In the case of only one piece ($N = 1$), equations (2.10) and (2.11) will be exactly identical to equations (2.10) and (2.11) in WZ03.

It should be noted that, in deriving equations (2.8) and (2.9) and subsequently equations (2.10) and (2.11), there is no use of the smallness of ψ' or ϕ' with respect to $\bar{\Psi}$

and $\bar{\Phi}$. The only requirement in deriving these equations so far is that $\bar{\Psi}$ and $\bar{\Phi}$ will be solution of equations (2.4) and (2.7), and equations (2.10) and (2.11) will then follow automatically without appealing to the concept of mean and perturbation. *The validity of equations (2.8), (2.9), (2.11) and (2.12) is always assured if the mean fields $\bar{\Psi}$ and $\bar{\Phi}$ are chosen to satisfy equations (2.4) and (2.7) a priori.* In this sense, the concept of means and perturbations will no longer exist, and we still have the system of piecewise PV inversion.

Chapter 3. Boundary conditions

As we know, PV inversion is basically a boundary value problem. The philosophy of piecewise PV inversion will consist of two key steps: 1) separate the total geopotential ϕ , streamfunction ψ , and potential vorticity Q into means and perturbations, 2) select a PV piece Q'_i out of the total PV anomaly Q' to perform an inversion. It is necessary to distinguish two different types of problems

a) *Given the total PV anomaly Q' with all boundary conditions associated with Q' , it is required to partition Q' into N pieces and then find the 3D balanced fields ψ'_k and ϕ'_k associated with a selected PV piece Q'_k .*

b) *Given N PV pieces Q'_i ($i = 1 \dots N$) with the appropriate boundary conditions for each piece Q'_i , it is required to find the 3D balanced fields ψ'_k and ϕ'_k associated with a selected PV piece Q'_k*

To facilitate our subsequent discussion, the former case is named “partitioning piecewise” (PP) and the later case will be named “superposition piecewise” (SP). In many applications, the PP problem is encountered more frequently. We now examine each problem separately.

PP problem

For the sake of clarity, consider an operator L acting upon two unknown functions ϕ'_1 and ϕ'_2 with appropriate boundary conditions as follows⁴:

$$L(\phi'_1) = F_1, \quad \phi'_1|_{\text{boundary}} = \varphi_1 \quad (3.1)$$

$$L(\phi'_2) = F_2, \quad \phi'_2|_{\text{boundary}} = \varphi_2 \quad (3.2)$$

⁴ it is immediate to generalize to an arbitrary number of unknown functions without any significant changes

where F_1 and F_2 are two given forcing functions, φ_1 and φ_2 are also given functions. Consider next a new unknown function ϕ'_3 that is the solution of the same operator L for which the forcing function of ϕ'_3 is given by the sum of the forcing functions of (11a,b), i.e., $F_3=F_1+F_2$, but the boundary of ϕ'_3 is an unknown function φ_3

$$L(\phi'_3) = F_1 + F_2, \quad \phi'_3|_{\text{boundary}} = \varphi_3 \quad (3.3)$$

A question now is that whether $\phi'_3 = \phi'_1 + \phi'_2$. In general, solution ϕ'_3 will not be equal to the sum of ϕ'_1 and ϕ'_2 . The equality occurs if and only if:

$$\text{iv) } L(\phi'_1) + L(\phi'_2) = L(\phi'_1 + \phi'_2) \quad (C1)$$

$$\text{v) } \varphi_3 = \varphi_1 + \varphi_2 \quad (C2)$$

$$\text{vi) } \text{Solution of equation: } L(\phi') = F \text{ exists and is unique} \quad (C3)$$

The first condition is usually referred to as the linearity of operator L . In piecewise PV inversion problem, equations (2.4) and (2.7) are nonlinear and it seems to be that this linearity condition is not satisfied. However, the piecewise method developed by DE91 guarantees that condition (C1) is held. Condition (C2) is assured if the homogenous boundaries for all pieces are used, *but it will be not valid in general*. Note that nothing has been mentioned about condition (C3) so far because it is virtually impossible to answer theoretically. We will assume that condition (C3) is valid without any justification as mentioned in the introductory section. As a matter of fact, this condition can be checked experimentally by changing model parameters, grid mesh, initial guess, etc, to see whether the balance system converges to the same solution.

In some applications, the homogeneity of boundary conditions is so strict and needs to be relaxed. *For the PP problem, the total boundary condition φ_3 for ϕ'_3 is given while the boundary conditions φ_1 and φ_2 could be unknown*. Evidently, there are an infinite number of

ways to divide the boundary condition φ_3 into φ_1 and φ_2 such that the sum of φ_1 and φ_2 is equal to φ_3 . The problem of partitioning boundary conditions now becomes very arbitrary. In DE91, they employed the homogenous lateral boundary conditions for all PV pieces and their partition therefore always guarantees the superposition principle. A question is: In case the boundary conditions are inhomogeneous, how can we partition the total boundary condition in a meaningful way? In this work, we handle the boundary conditions for the PP problem in the following way: we first divide the problem:

$$L(\phi') = F, \quad \phi' \Big|_{\text{boundary}} = \varphi \quad (3.3)$$

into two small problems:

$$L(\phi_h') = F, \quad \phi_h' \Big|_{\text{boundary}} = 0 \quad (3.4)$$

$$L(\phi_o') = 0, \quad \phi_o' \Big|_{\text{boundary}} = \varphi \quad (3.5)$$

The piecewise PV partitioning is then applied for the homogeneous boundary problem only (i.e. problem 13a). In this case, the sum of all perturbation fields ψ'_i and ϕ'_i ($i = 1, \dots, N$) obtained by performing inversion of each piece Q'_i will not equal to the perturbation (ψ', ϕ')

inverted from $Q' = \sum_{i=1}^N Q'_i$, but it is equal to (ψ'_h, ϕ'_h) , which is inverted from $Q' = \sum_{i=1}^N Q'_i$ with

homogenous boundary conditions. The difference between $\sum_{i=1}^N (\psi_i, \phi_i)'$ and (ψ', ϕ') is given by

the solution of (3.5). In most of the practical cases, this difference is small if the domain is large enough (Shapiro 1996), but the difference between the sum $\sum_{i=1}^N (\psi, \phi)'_i$ and (ψ', ϕ')

could be large when the boundary effects are significant.

SP problem

Unlike PP problem in which the total boundary condition ϕ_3 is given and both ϕ_2 and ϕ_3 are unknown, the boundary conditions ϕ_1, ϕ_2 are given for SP problem. This makes the SP problem simpler and much less arbitrary than the PP problem. All we need to do is to perform an inversion of operator L right away for ϕ_1' and ϕ_2' . To find ϕ_3' , we just take the sum $\phi_1 + \phi_2$ as the boundary and $F_1 + F_2$ as forcing function for ϕ_3' and perform an inversion. The superposition principle will be satisfied automatically.

The most common lateral boundary conditions used for piecewise PV inversion are: Dirichlet boundaries for ψ' and ϕ' along the lateral boundaries, where ϕ' matches the simulated output (or from observations) and ψ' will be given by:

$$\frac{\partial \psi'}{\partial s} = -V_h \cdot n + \frac{\oint V_h \cdot n \cdot dl}{\oint dl} \quad (3.6)$$

where l is a path along the lateral boundaries, s is vector tangent to that path and \mathbf{n} is a normal vector of that path. The bottom ($z = z_B$) and top ($z = z_T$) boundaries for ψ' and ϕ' will be given by Neumann conditions:

$$\left. \frac{\partial \phi'}{\partial z} \right|_{z=z_B} = g \frac{\theta'_B}{\theta_0} \quad \left. \frac{\partial \phi'}{\partial z} \right|_{z=z_T} = g \frac{\theta'_T}{\theta_0} \quad (3.7)$$

(see DE91 or WZ03 for more detail)

Chapter 4. Calculations of mean fields

In order to make piecewise PV inversion more versatile, the problem of how to calculate the mean fields $\bar{\Psi}$ and $\bar{\Phi}$ will be addressed further in this chapter. There are several ways to perform this task. For example, DE91, Wu and Emanuel (1995a,b) used a temporal average over a period of 5 days of PV field to obtain the mean PV \bar{Q} . Eqs. (2.4) and (2.7) will then be iterated until they converge to obtain $\bar{\Psi}$ and $\bar{\Phi}$ in the whole domain. In a different way, WZ03, Shapiro (1996), Shapiro and Franklin (1999) obtained the balanced field by first taking the azimuthal average of $\bar{\Psi}$. The balance equation (2.4) is then inverted to obtain $\bar{\Phi}$, and finally \bar{Q} is calculated from Eq. (2.7). In this way, the fields $\bar{\Psi}$ and $\bar{\Phi}$ are automatically in balance. However, as noted in WZ03, this latter approach, when applied to hurricane studies, may lead to negative static stability near the top of the PBL where the tangential wind is maximized and the inversion for ψ' and ϕ' therefore may not converge. Another point is that the azimuthal average, as applied to hurricanes, results in a mean field possessing nearly all the mean characteristics of hurricanes. For example, the mean tangential wind is the same order of magnitude as the total field. This method thus gives a small residual perturbation after subtracting the mean PV field from the total PV field.

However, if one is interested in the contribution of a PV in the core region of a hurricane, this kind of average would not be useful. In this work, we suggest an alternative way to obtain the balanced mean fields. Instead of taking the azimuthal average of streamfunction $\bar{\Psi}$, we first take the running mean of Φ so that the mean field $\bar{\Phi}$ is nearly flat (of no hurricane character). The reason for using running means is because we can control

the flatness of $\bar{\Phi}$ flexibly. Recall that the perturbation ϕ' would have been a small residual after subtracting the azimuthal-average from the total field. We next invert $\bar{\Psi}$ from $\bar{\Phi}$ by using NLB equation (2.4). This kind of inversion needs a special treatment as follows:

From equation (2.4)

$$\nabla^2 \Phi = \nabla(f \nabla \psi) + 2J \left(\frac{\partial \psi}{\partial x}, \frac{\partial \psi}{\partial y} \right) + \nabla F_f \quad (4.1)$$

We first expand (4.1) as:

$$\nabla^2 \Phi = f \nabla^2 \psi + \frac{\partial f}{\partial x} \frac{\partial \psi}{\partial x} + \frac{\partial f}{\partial y} \frac{\partial \psi}{\partial y} + 2 \left(\frac{\partial^2 \psi}{\partial x^2} \frac{\partial^2 \psi}{\partial y^2} - \left(\frac{\partial^2 \psi}{\partial x \partial y} \right)^2 \right) + \nabla F_f \quad (4.2)$$

Rewrite the fourth term on the right hand side of (4.1) as follows:

$$\frac{\partial^2 \psi}{\partial x^2} \frac{\partial^2 \psi}{\partial y^2} = \frac{1}{4} \left[\left(\frac{\partial^2 \psi}{\partial x^2} + \frac{\partial^2 \psi}{\partial y^2} \right)^2 - \left(\frac{\partial^2 \psi}{\partial x^2} - \frac{\partial^2 \psi}{\partial y^2} \right)^2 \right] \quad (4.3)$$

plugging (4.3) into (4.2) and rearranging it gives

$$(\nabla^2 \psi)^2 + 2f \nabla^2 \psi + 2 \left(\frac{\partial f}{\partial x} \frac{\partial \psi}{\partial x} + \frac{\partial f}{\partial y} \frac{\partial \psi}{\partial y} \right) - \left(\frac{\partial^2 \psi}{\partial x^2} - \frac{\partial^2 \psi}{\partial y^2} \right)^2 - \left(4 \frac{\partial^2 \psi}{\partial x \partial y} \right)^2 + 2 \nabla F_f - 2 \nabla^2 \phi = 0 \quad (4.4)$$

This is a quadratic equation of Laplacian of ψ . Therefore, we can solve for $\nabla^2 \psi$ to yield:

$$\nabla^2 \psi = -f + \left\{ f^2 + \left(\frac{\partial^2 \psi}{\partial x^2} - \frac{\partial^2 \psi}{\partial y^2} \right)^2 + \left(2 \frac{\partial^2 \psi}{\partial x \partial y} \right)^2 + 2 \nabla^2 \phi - 2 \nabla F_f - 2 \left(\frac{\partial f}{\partial x} \frac{\partial \psi}{\partial x} + \frac{\partial f}{\partial y} \frac{\partial \psi}{\partial y} \right) \right\}^{\frac{1}{2}} \quad (4.5)$$

The plus sign is chosen since it results in an familiar geostrophic approximation: $\nabla^2 \Psi = \nabla^2 \Phi / f$. Equation (4.5) will then be solved iteratively,

$$\nabla^2 \psi^{n+1} = -f + \left\{ f^2 + \left(\frac{\partial^2 \psi^n}{\partial x^2} - \frac{\partial^2 \psi^n}{\partial y^2} \right)^2 + \left(2 \frac{\partial^2 \psi^n}{\partial x \partial y} \right)^2 + 2 \nabla^2 \phi - 2 \nabla F_f - 2 \left(\frac{\partial f}{\partial x} \frac{\partial \psi^n}{\partial x} + \frac{\partial f}{\partial y} \frac{\partial \psi^n}{\partial y} \right) \right\}^{\frac{1}{2}} \quad (4.6)$$

The iteration will converge when $|\Psi^{n+1} - \Psi^n|$ is less than some limitation. The convergent condition for this equation is

$$f^2 + 2\nabla^2\Phi > 0 \quad (4.7)$$

Experiments with hurricane Bonnie showed that there is less than 10% of total grid points at which this condition is not valid at the first iteration.

After obtaining the mean streamfunction $\bar{\Psi}$ from $\bar{\Phi}$, the mean PV field \bar{Q} is computed using equation (2.7). All fields are automatically in balance without performing an inversion of both Eqs. (2.4) and (2.7) as in previous studies. It should be noted that although it is not required to perform an inversion of Eqs. (2.4) and (2.7), this does not mean that there are no need of boundary conditions. The boundary conditions will enter in calculating the mean PV field \bar{Q} . This is because by using (2.7) to calculate \bar{Q} the calculation will be restricted to the inside points only. To complete the value for \bar{Q} at boundaries, boundary conditions are required. The advantage of this method is that we can make, in principle, the mean fields $\bar{\Phi}$ as flat as we want, depending on each specific situation. This allows us to investigate the PV anomaly more effectively since it is feasible to separate a large perturbation PV piece in the same dynamically balanced way as in the previous studies.

Chapter 5. New methodology of piecewise inversion

As mentioned in Chapter 1, the piecewise inversion technique used in DE91 has a main obstacle: the number of equations required to be solved increases as twice as the number of PV pieces. The large nonlinear equations system does not guarantee the convergence and stability of the solution. As presented in DE91 and more detailed in Shapiro (1996), the piecewise inversion system [i.e., Eqs. (2.10) and (2.11)], consisting of $2N$ equations for N pieces, will be iteratively solved. This iteration turns out to be very sensitive to model parameters such as the underrelaxing factor, the scaling dimensional numbers, the stability parameter, the threshold for PV magnitude, the free parameter ε in WZ03's method, etc. This is because *it is necessary to take into account not only the convergence of each equation but also the convergence of the whole system of $2N$ equations*. In this work, we propose a new algorithm to deal with piecewise PV inversion with an arbitrary number of pieces. Our purpose is to find a way to solve for Eqs. (2.10) and (2.11) so that the piecewise PV inversion technique is more applicable.

Our methodology is based on one key property of piecewise inversion; that is, *the sum of all perturbations obtained by inverting each piece Q'_i must be equal to the perturbations obtained by inverting the sum of all PV piece Q'_i , i.e.*

$$\psi' = \sum_{i=1}^N \psi'_i \text{ and } \phi' = \sum_{i=1}^N \phi'_i \text{ for } Q' = \sum_{i=1}^N Q'_i$$

where ψ'_i and ϕ'_i ($i = 1 \dots N$) are inverted from Q'_i , and ψ' and ϕ' are inverted from Q' . With this remark, instead of solving $2N$ equations of type (2.10) and (2.11) simultaneously, we carry out the following procedure:

- Step 1: We first use the system of equations for one PV piece developed by WZ03 to solve for ψ' and ϕ' in which the PV piece is Q' with the full boundary conditions as noted in Chapter 4.

- Step 2: Replacing all of the summations of derivatives of ψ'_i and ϕ'_i in (2.10) and (2.11) by the same derivatives applied for ψ' and ϕ' , respectively, e.g.

$$\sum_{n=1}^N \frac{\partial^2 \psi'_n}{\partial x \partial y} \longrightarrow \frac{\partial^2 \psi'}{\partial x \partial y}, \quad \sum_{n=1}^N \frac{\partial^2 \psi'_n}{\partial x \partial z} \longrightarrow \frac{\partial^2 \psi'}{\partial x \partial z}, \quad \sum_{n=1}^N \frac{\partial^2 \psi'_n}{\partial z \partial y} \longrightarrow \frac{\partial^2 \psi'}{\partial z \partial y} \dots \text{etc.}$$

and similarly for all other derivatives of ϕ'_n . Note that at this step, ψ' and ϕ' are known from step 1 above.

- Step 3: Solving both equations (2.10) and (2.11) for each selected PV piece Q'_i with its appropriate boundary conditions, provided that the sum of boundaries of all PV pieces Q'_i will be equal to the boundary conditions of the total PV anomaly Q' . The boundary issue will become much simpler (and less arbitrary) if the boundary of the total PV anomaly Q' is homogeneous. In this case, the boundary condition of all pieces Q'_i is simply homogeneous as discussed in detail in Chapter 4. By carrying out this procedure, there is no requirement for knowing ψ'_j and ϕ'_j ($j \neq i$) in advance because they are already included in ψ' and ϕ' , which have been calculated from step 1. Therefore, the system (2.10) and (2.11) is closed for ψ'_i and ϕ'_i , and it is only necessary to solve for the i -th PV piece.

This procedure is particularly simple and is not involved in an annoying process of solving $2N$ equations all together. By following this way, it is possible to invert any PV piece no matter how many pieces they are (N can be very large).

PART II. APPLICATION TO HURRICANE BONNIE (1998)

Chapter 6. Overview of Hurricane Bonnie

Hurricane Bonnie (1998) originated from the West coast of Africa on 14 August 1998. After a five-day development, it reached a tropical depression stage with central pressure falling below 1009 hPa. It became category-1 hurricane on 0600 UTC 22 August and moved west-northwestward under the influence of the Bermuda high. Bonnie then deepened rapidly with time, reaching the minimum pressure of 954 hPa two days later. Zhu et al. (2004) obtained a 5-day successful simulation of Hurricane Bonnie (1998) with the triply nested-grid (36/12/4 km) version of the PSU/NCAR (MM5, V3.4) model that covers the initial rapid deepening, steady variation and landfalling stages of the storm. The simulation reproduces reasonably well the track, intensity change and asymmetric inner-core structures of the storm, including a partial eyewall and an eyewall replacement cycle.

To have some general ideas of how PV comes into play in the whole development of hurricanes and to what extent PV is capable of characterizing the different stages of the development, it is necessary first to examine some PV structures and its evolution with time. Figure 1 shows the time evolution of maximum surface wind, minimum sea-level pressure, and the mass-weighted storm-scale PV for the 5-day simulation, initialized at 0000 UTC 22 August. The model captures well a slow deepening period in the first 36 h, a rapid deepening stage from 36 h to 54 h, a quasi-steady stage from 54 h to 102 h, and finally a weakening stage after landfall (see Zhu et al. 2004 for details). It is evident from this figure that hurricane intensity changes could be consistently represented by PV, a view that is recently received more attention (Chen and Yau 2001, Yau et al. 2004). Of interest is that during the

period of 24 h to 48 h, PV averaged within a core region of Bonnie keeps intensifying while there is little source of heating. It is expected from the equation of PV that the PV in the eye should be unchanged or at most decrease with time under the influence of (numerical diffusive) frictional effects. A calculation of the contribution of the eddy terms in PV budget equation revealed that the eddy fluxes associated with wave activities are the main factor in intensifying PV at the center of a hurricane (Fig. A1a). Under the strong influence of northwesterly shear during the intensifying stage (24 h to 48 h), eddy fluxes tends to be negative (inward flux) at the upshear side and positive at the downshear side as shown in Fig. A1b. The total flux is slightly negative which indicates the total inward flux of PV at the center. The eddy fluxes of PV calculated above, however, contains wave activities over the whole domain including: Vortex-Rossby waves propagating around the eyewall, gravity waves propagating radially, or the combinations of both waves as studies in Schecter and Montgomery (2004). By using piecewise PV inversion, it is possible to qualify specifically how much a Vortex-Rossby waves propagating around the eyewall where PV is constantly generated due to convection will contribute to the PV intensification at the center.

It should be particularly remarked here that the eddy fluxes calculated from PV inversion are different radically from the fluxes using simple perturbations as the differences between total and mean. The eddy fluxes based on PV inversion are associated exclusively with a selected piece of PV anomaly. Therefore, eddy fluxes from PV inversion will be in balance (i.e. persist for a long time), whereas the eddy fluxes from simple perturbation calculations is instantaneous. Model results show that PV was continuously generated by the eyewall convection during this maintenance stage but not immediately advected into the core region. To see this point, Fig. 2 shows the snapshots of PV distribution at 45-minute intervals

at level $z = 3$ km at 0200 UTC 25 August. A large volume of PV is concentrated in the eye, accounting for the intensity of storm-scale rotation. A few isolated PV anomalies could be seen in the eyewall. Because of the strong forcing of large-scale northwesterly shear (see Fig. 3), cloud convection, as indicated by the latent heating rates and radar reflectivity, occurs mostly in the northeast quadrant of the eyewall, i.e., on the downshear-left, which is consistent with the conceptual model of Black et al. (2002). This shear tends to provide favorable upward motion on the downshear side, i.e., in the southeast quadrant (Wang and Holland 1996; Frank and Ritchie 1999; Zhang and Kieu 2005). More clouds develop on the downshear-left because of the growth and downstream advection of cloud condensates, where PV anomalies are generated and advected mostly around the eye rather than directly into the eye. This conclusion can also be seen from the radar reflectivity in Fig. 4, which characterizes evidently the appearance of clouds.

To gain insight into the 3D structures of PV, an East-West cross section through Bonnie's center and an azimuthal-height cross section at the RMW of both PV and PV anomaly are given in Figs. 5 and 6, respectively. Apparently, both PV and PV anomaly show pronounced asymmetries with high PV in the northeast quadrant where deep convection and vertical motion are intense. One remarkable feature that can be easily seen from Figs. 5 and 6 is the downshear tilt of the stripes of PV maximum/minimum with height with the wavenumber-1 structures. This seems to be explained by the impact of the sheared flow in the eyewall, i.e. the stronger advectations of tangential winds at the lower levels than those at the upper levels. However, if this is the case, the region of maximum PV anomaly at the lower levels will move faster than that at the upper level after a while and will result in both a downshear tilt and an upshear tilt alternatively when the lower PV maximum moves around

the eyewall. A time series of azimuth-height cross section of PV, nevertheless, indicates mostly the upshear tilt of PV pattern and the above argument based on sheared flow of tangential wind is thus incomplete. A second mechanism is believed due to the large-scale northwesterly shear. As seen in Fig. 6, PV anomaly is continuously generated at the middle levels and then advected downward at the NW quadrant *under the influence of large-scale northwesterly vertical shear*, where vertical motion is downward at upshear side as pointed out in Zhang and Kieu (2005). This mechanism depends critically on the asymmetry of vertical motion around the eyewall and will no longer valid in the case there is a uniform upward motion all around the eyewall and no large scale vertical shear. If this explanation is right, it can be anticipated that for a strong hurricane with upward motion all around the eyewall with no environmental shear, there should have both the upshear and downshear tilts of PV with height alternating with time because the tangential advection now is the only mechanism.

The most attractive stage of Bonnie's lifetime, which is the main concentration in our work here, is an eyewall replacement process occurring between 86h and 96 h of model simulation during which there appeared double eyewalls. A motivating question is whether PV variable has capability of capturing this important stage and, if so, how PV can provide some understandings to this replacement mechanism. Fig. 8 shows the PV evolution during the eyewall replacement stage starting from 88h. One can notice evidently a PV concentration at the center as well as a distinct PV ring at the outer eyewall, which represents well the double eyewalls during this stage. The outer PV ring is quite faint at 1615 UTC August 26, and then becomes more and more organized as it propagates cyclonically, and finally attains its clear outer ring about 2 hours later. A further noteworthy feature of PV

evolution is that the replacement process lasted only 2 to 3 hours starting from 1600 UTC August 26. After that the PV concentration within the eye tends to disperse outward as shown in Fig. 8. The vertical East-West cross-sections of PV corresponding to Figs. 7b and 8b are given in Fig. 9. They reveal a monopolar structure of PV with the maximum PV concentrating at the center around middle levels. The mechanism for this replacement process has not been addressed in detail so far and will be presented in the next chapter. It should be noted that the monopolar structure of PV after 96h is somewhat the same as that in dry-run experiment in Chen and Yau (2001). However, this similarity can not be taken further because in their experiment there is no source of latent heat release, while in our simulation the convective processes play an important role.

Chapter 7. Piecewise PV inversion

In this chapter, the techniques developed in Chapters 2 and 5 will be applied to Hurricane Bonnie (1998) to examine some possibilities responsible mainly for the eyewall replacement process mentioned in Chapter 6 (Fig. 7). This will prove the applicability of piecewise PV inversion technique developed in Part I to hurricane studies. The model outputs of Hurricane Bonnie, which are described briefly in Chapter 6, will be chosen for this study. The 4 km-resolution outputs consist of 163×163 grid points in (x, y) plane and 23 uneven σ levels. For our piecewise PV inversion program, we restrict the original domain to a smaller domain with 97×97 grid points in (x, y) plane around the hurricane center and interpolate from 23 uneven σ levels to 33 even levels in pseudo-height coordinate. More detailed descriptions can be found in WZ03. As discussed in Chapter 6, the piecewise PV inversion is expected to offer some mechanisms for the transitional stage from double eyewall at 86h (Fig. 7) to eventually a ring of outer PV as in Fig. 8 after 96h of simulation. The verifications of our new scheme for inversion are presented in the appendix for the clarity.

The time slice at 1700 UTC August 16 will be chosen for our purpose because the outer PV ring has the most distinct separation from the PV at the center, and the ring is nearly close. A portion of PV at the eastern side is selected and will be regarded as a piece of PV anomaly. The remaining will be treated as a second PV piece. Of course, there is nothing preventing us from choosing the whole PV ring to work with. However, a portion of PV ring will be more realistic and meaningful as in practical situation a PV ring is barely closed completely. It is important to note here again that if PV anomaly is defined as a difference between the total PV and azimuthal average, the PV anomaly is then just a small residual and

it is not possible to obtain the whole outer PV ring to invert (see chapter 4 for more detailed). In our work, the outer PV ring will *not be taken as the difference between total and azimuthal average but simply cut out of the total PV* and treated as a piece of PV anomaly superimposed on a balanced vortex. Fig. 10 shows the perturbations of pressure, potential temperature, and vertical motion associated with this PV piece at $z = 3$ km (the same general patterns are also obtained at all lower levels and only level $z=3$ km is thus provided). Vertical motion and divergent winds in Fig. 10c are obtained by solving the omega equation *without heating and frictional effects* (see Zhang and Kieu 2005). This running option provides a clear picture of the sole impacts of outer PV on secondary circulation. One notices immediately from Fig 10a that the outer positive PV produces a very deep low pressure region with cyclonic wind confined closely to the outer PV ring. The stronger the PV anomaly, the deeper the pressure perturbation and the stronger the rotational wind field. This is nothing new but a consequence of the elliptic property of the PV system (cf. Eqs. 2.10 and 2.11). It is well-known that for a Laplacian operator acting on a function, a positive forcing will correspond to a negative value of the function everywhere, provided that the boundaries are all homogeneous. In the case of piecewise PV system, the ellipticity of equation (2.11) is always checked during iteration process to guarantee the convergence of both Eqs. (2.10) and (2.11) (the points where the elliptic condition are not satisfied will be adjusted immediately). Therefore, the positive PV anomaly on the RHS of (2.11) will be certain to give the negative perturbation geopotential height, which is then converted to pressure perturbation. It is familiar that the low pressure system will result in cyclonic motion, and the cyclonic circulation in Fig. 11a once again acknowledges this common truth. Note particularly that the southly wind at the inner side of the PV ring will compensate the rotational wind inside the

ring (but outside the inner eyewall) while the northerly wind at the outer side will enhance the rotational wind outside the ring. This explains why the appearance of an outer PV ring enclosing a pre-existing hurricane eye will subsequently weaken rotational wind and consequently vorticity inside this ring.

A second noteworthy feature of the outer PV ring is the warming anomaly inside and cooling anomaly outside the ring as shown in Fig. 10b. One usually expects intuitively to see the warming anomaly everywhere in order to be consistent with the development of low pressure system in Fig. 10a. What have happened with the cooling effect outside the PV ring? The nature of this interesting feature roots in the fact that the outer PV ring has radius increased with height (Figs. 11a and 12a). As observed in Fig. 10a, the maximum in magnitude of pressure perturbation occurs within the PV ring. Therefore, there will have a deep low pressure system right above the outside of PV ring at $z = 3$ km (Fig. 11a), which is best seen from the outward tilt of the low center of pressure perturbation (Fig. 12a). This deep low system aloft results in a positive potential temperature at the upper level so strong that the outer side of PV ring at the lower levels must cool down to offset the large expansion of the column of air aloft (Figs. 13b, 12b and 11b). Pictorially, we can imagine that the upper column expands larger than the shrink at the lower level so that, totally, there still has an expansion of the whole column of air, consistent with the existence of the low pressure system at the surface.

A question now is that what is the consequence of this *warming inside and cooling outside*⁵ effect as seen in Fig. 10b. Interestingly, the warming inside tends to expand the warm core (enlarge the bow shape of isentropic surface), while the cooling outside tends to

⁵ To avoid a lengthy expression, inside and outside here are always meant inside and outside of the outer PV ring in question.

sharpen the core region (maintain subsequently the bow shape). Without cooling outside, the bow shape of the isentropic will spread out and the bow shape will be shallower, leading to the disappearance of warm core. *The warming inside and cooling outside together with the enhancement outside and reducing inside of rotational winds are believed, from the point of view of our piecewise PV inversion, to be one of the main mechanisms responsible for the eyewall replacement process and for the gradual disappearance of the PV at the center region at the later time.*

Besides the major impacts of the perturbation rotational winds and warming/cooling effects discussed above, the PV outer ring also induces significant divergent winds and vertical motion as well. These circulations are obtained by using the omega system, which is employed in our recent work to study the impacts of shear on secondary circulation (see appendix). Fig 10c shows the vertical motion induced by the outer PV ring superimposed by divergent wind. Evidently, the PV ring results in a considerable vertical motion (up to 0.7 m/s), which enhances convection activity significantly within the ring. The alternative upward and downward motions in Fig. 10c are due to the non-uniformity of the PV distribution within the ring (see shaded area in Fig. 10). Correspondingly, upward/downward motion is associated with convergent/divergent wind at the lower levels as seen in Fig. 10c (The opposite situation: divergent/convergent winds associated with upward/downward motions is also observed at the upper levels but not shown here). It is the dominance of the convergent winds and vertical motion within the ring that help maintain and intensify the newly appeared outer eyewall. If we say perturbation potential temperature and wind fields are responsible for broadening the eye, then it is the convergent wind and vertical motion

within in ring that leads to the large concentration of PV around the outer ring at the later time as seen in Fig. 8

The second interesting question of how the PV at the core of Bonnie keeps increasing and why there is no source of heating (Fig.1c) was also attempted in our work but will be mentioned briefly here only for the purpose of completeness. As we know, PV is expected to be conserved in the absence of heating and friction. Within the eye, there is no source of latent heat released and it is expected that PV inside the eye core should not be changed significantly or at most decrease with time due to frictional effect. However, as seen in Fig. 1c, PV averaged within eye core region follows quite closely to the general development of Bonnie, with a steady increase from beginning up to 48 h before decreasing. Piecewise PV can provide the balanced perturbation winds associated with a specific PV piece, which can be used to calculate eddy fluxes of momentum and vorticity specifically for this piece only. Though the second question of wave activities is not our main concentration, it is worthy to note that our piece PV inversion *does* offer an answer for this interesting question. As a matter of fact, Montgomery and Kallenbach (1997) have addressed this question through a series of theoretical developments of Vortex-Rossby wave as well as their subsequent numerical experiments (Montgomery and Kallenbach 1997; Moller and Montgomery 1998; Schechter and Montgomery 2004). In connection with their work, it is also possible to see the wave activities on the mean PV within the core of a hurricane from our work. Explicitly, one may ask how much a piece of PV anomaly within the eyewall will contribute to the eddy fluxes of vorticity. Some experiments with our new piecewise PV inversion system have supported a conclusion that it is the PV anomalies around the eyewall which are generated constantly by convection that account for most of the eddy fluxes of vorticity.

During the intensifying stage of a hurricane, convective heating generates new PV in the eyewall, and this will indirectly influence the PV inside the eyewall, resulting in the change of PV as seen in Fig. 1c (dash curve). Here, we can see this mechanism again in the light of PV inversion, which gives us specifically how much a PV piece will contribute to the balanced eddy flux. Note that eddy fluxes obtained from PV inversion are calculated (this will be included in this part, as discussed) based on balanced perturbation winds, which are very different from perturbations taken simply as the difference between total fields and azimuthally average. The latter perturbations are not in balance. Several further steps need to be conducted before a final conclusion can be obtained and we would like to point out here that piecewise PV inversion is a very useful and appropriate tool for this purpose.

Chapter 8. Summary and conclusions

In this work, a system of equations for piecewise PV inversion, which employs the WZ03's technique, with an arbitrary number of pieces is developed in Chapter 2. This WZ03's technique has an advantage of introducing a free parameter ε to control the convergence of the system of nonlinear PV equations, which is especially suitable when applied to hurricane researches. However, their PV system so far has been applied to the case of one PV piece only, and their technique is extended from one PV piece to an arbitrary number of pieces in this work. We next propose an algorithm to handle the problem of solving the piecewise PV system for the case of many PV pieces. The traditional approach to solving piecewise PV system is to follow DE91's methodology in which the system of $2N$ nonlinear balanced equations needs to be simultaneously iterated. The weakness of iteration method lies in its convergence and stability, especially when there are more than three PV pieces. Our new approach overcomes particularly this difficulty, which makes piecewise PV inversion become more practical in applications. Third, a systematical treatment of boundary problem was presented in Chapter 3, which so far has not been addressed fully in previous studies. Finally, an alternative way of determining mean balanced fields is also mentioned, which allows us to separate meaningfully a perturbation PV piece to investigate (Chapter 4).

These new developments are then applied to examine the mechanisms accounting for eyewall replacement process that was explicitly captured in a simulation of Hurricane Bonnie (1998) with the finest mesh of 4km. By treating the outer PV ring as a piece of PV anomaly superimposed on a balanced vortex and the remaining PV anomaly as a second piece, we have obtained some results that provide detailed insights to the transitional stage from double

eyewall to a single eyewall at the later time. Specifically, perturbation rotational winds associated with the outer PV ring will weaken tangential winds within the annulus created by the inner eyewall and outer PV ring. In the meantime, perturbation potential temperature warms the region between the inner edge of the PV ring and the outer edge of inner eyewall and thus enlarges the bow shape of isentropic surface at the low levels. On the other hand, the cooling effect of perturbation potential temperature will sharpen this bow shape. Under these impacts of both perturbation winds and potential temperature, the inner eyewall tends to be weakened and dispersed outward. The vertical motion and divergent winds induced by the outer PV ring will subsequently draw the entire moisture source into the outer PV ring, leading to a new larger eyewall replacing the inner eyewall inside.

It should be particularly noted that our results offer explanations for the eyewall replacement process *only after the outer eyewall has some initial appearance*. Once the outer PV ring appears, it will quickly grow to full outer eyewall and weaken the inner eyewall no matter how weak the outer PV ring is. Our results do not provide an answer for why and how some initial PV ring appears. This initial appearance of outer PV ring may be due to some spontaneous processes or Vortex-Rossby waves propagating radially and azimuthally.

Appendix 1: Omega system

The ω -equation in the vertical upward-pointing, pseudo-height z -coordinates (Hoskins and Bretherton 1972), including the water loading effects, is given by (see Wang and Zhang 2003)

$$\begin{aligned}
 & \nabla^2 \left(\frac{\partial^2 \phi}{\partial z^2} \omega \right) + f \eta \frac{\partial}{\partial z} \left\{ (z_a - z)^{-\mu} \frac{\partial}{\partial z} [(z_a - z)^\mu \omega] \right\} - f \frac{\partial}{\partial z} \left(\frac{\partial \omega}{\partial x} \frac{\partial^2 \psi}{\partial x \partial z} + \frac{\partial \omega}{\partial y} \frac{\partial^2 \psi}{\partial y \partial z} \right) \\
 & \quad - f \frac{\partial}{\partial z} \left(\frac{\partial \omega}{\partial x} \frac{\partial^2 \chi}{\partial y \partial z} - \frac{\partial \omega}{\partial y} \frac{\partial^2 \chi}{\partial x \partial z} \right) - \left(f \frac{\partial \eta}{\partial z} \frac{\mu}{z_a - z} + f \frac{\partial^2 \eta}{\partial z^2} \right) \omega \\
 & = f \frac{\partial}{\partial z} [\mathbf{V}_h \cdot \nabla \eta] - \nabla^2 [\mathbf{V}_h \cdot \nabla \frac{\partial \phi}{\partial z}] - \beta \frac{\partial^3 \psi}{\partial t \partial y \partial z} - 2 \frac{\partial^2}{\partial t \partial z} \left(\frac{\partial^2 \psi}{\partial x^2} \frac{\partial^2 \psi}{\partial y^2} - \frac{\partial^2 \psi}{\partial x \partial y} \frac{\partial^2 \psi}{\partial x \partial y} \right) \\
 & \quad + \frac{g}{\theta_0} \nabla^2 \dot{q} - f \frac{\partial}{\partial z} \left(\frac{\partial f_y}{\partial x} - \frac{\partial f_x}{\partial y} \right) - \frac{\partial^2}{\partial t \partial z} \left(\frac{\partial f_x}{\partial x} + \frac{\partial f_y}{\partial y} \right) \tag{A1}
 \end{aligned}$$

where ∇ is a horizontal gradient operator on constant pseudo-height surfaces, $\mu = C_v/R_d$ and $z_a = C_p \theta_0/g$; $\eta = \zeta + f$; ψ and ϕ are the balanced total streamfunction and geopotential height inverted from a given PV field; χ is the (quasi-balanced) velocity potential; $\mathbf{V}_h = \mathbf{V}_\psi + \mathbf{V}_\chi$ is the horizontal velocity including both the balanced (\mathbf{V}_ψ) and divergent (\mathbf{V}_χ) components (i.e., $\mathbf{V}_h = \bar{\mathbf{k}} \times \nabla \psi + \nabla \chi$); \dot{q} is the latent heating rate; f_x and f_y denote the boundary-layer and (small) numerical diffusion effects along the x - and y - axes, respectively; and all the other variables assume their typical meteorological meaning. Given fictional, heating terms, ψ , and ϕ , the omega equation consists of two unknowns: ω , $\partial \psi / \partial t$. To close the system, we need to appeal to the vorticity equation

$$\nabla^2 \frac{\partial \psi}{\partial t} = -\mathbf{V}_h \cdot \nabla \eta - \omega \nabla^2 \frac{\partial \psi}{\partial z} - \eta \nabla^2 \chi + \mathbf{k} \cdot \frac{\partial \mathbf{V}_h}{\partial z} \times \nabla \omega + \frac{\partial f_y}{\partial x} - \frac{\partial f_x}{\partial y}. \tag{A2}$$

where the velocity potential χ is related to vertical motion ω through the continuity equation,

$$\nabla^2 \chi = -(z_a - z)^{-\mu} \frac{\partial}{\partial z} [(z_a - z)^\mu \omega]. \quad (\text{A3})$$

Thus, Eqs. (1) – (3) form a closed set of equations in ω , χ and $\partial\psi/\partial t$ that can be iteratively solved to yield the quasi-balanced vertical motion and horizontal divergent winds or the FSCs,

Appendix 2. Verification of Piecewise PV inversion

It is necessary to demonstrate that our new numerical scheme for piecewise PV inversion is capable of recovering the superimpose principle as original developed by DE91. This principle is verified by taking the difference between *the sum of all perturbations associated with each PV pieces* and *the perturbations associated with the sum of all PV pieces* (See Chapter 5 for more detail). Perturbations here mean rotational winds, potential temperature and geopotential. The latter is usually expressed as pressure perturbation rather than using direct geopotential). The smaller the difference, the better our scheme. In the testing experiment, the total PV anomaly is partitioned into four pieces: positive PV anomaly inside the eyewall (P1), negative PV anomaly inside eyewall (P2), PV anomaly within the eye core (P3), and the remaining PV anomaly (P4). Figs. 10 and 11 show the differences in pressure perturbations and in potential temperature, respectively, associated with pieces P1, P2, P3 and P4. As once can easily notice, our new algorithm scheme is good at all levels within a high accuracy. The complete results of balanced perturbations associated with all four pieces are given in the figure appendix for they provide no essential information of the eyewall replacement.

Reference

- Chen Y.-S., and M. K. Yau, 2001: Spiral bands in a simulated Hurricane. Part I: Vortex Rossby Wave verification, *J. Atmos. Sci.*, **58**, 2128-2145
- Davis, C. A., 1992: Piecewise potential vorticity inversion. *J. Atmos. Sci.*, **49**, 1397–1411
- , and K. Emanuel, 1991: Potential vorticity diagnostics of cyclogenesis. *Mon. Wea. Rev.*, **119**, 424–439
- Frank, W. M., and E. A. Ritchie, 2001: Effects of Vertical Wind Shear on the Intensity and Structure of Numerically Simulated Hurricanes. *Mon. Wea. Rev.*, **129**, 2249–2269
- Gall, R. L., J. Tuttle, and P. Hildebrand, 1997: Small-scale Spiral bands observed in Hurricanes Andrew, Hugo, and Erin. *Mon. Wea. Rev.*, **126**, 1749–1766
- Huo, Z.-H., D.-L. Zhang, and J. R. Gyakum, 1998: An Application of Potential Vorticity Inversion to Improving the Numerical Prediction of the March 1993 Superstorm. *Mon. Wea. Rev.*, **126**, 424-436
- , D.-L. Zhang, and J. R. Gyakum, 1999a: The interaction of potential vorticity anomalies in extratropical cyclogenesis. Part I: Static piecewise inversion. *Mon. Wea. Rev.*, **127**, 2546–2561.
- , D.-L. Zhang, and J. R. Gyakum, 1999b: The interaction of potential vorticity anomalies in extratropical cyclogenesis. Part II: Sensitivity to initial perturbations. *Mon. Wea. Rev.*, **127**, 2563–2575
- Hoskins, B. J., M. E. McIntyre, and A. W. Robertson, 1985: On the use and significance of isentropic potential vorticity maps. *Quart. J. Roy. Meteor. Soc.*, **111**, 877–946
- Jones S. C., 1995: The evolution of Vortices in Vertical Shear. I: Initially barotropic Vortices, *Q. J. R. Meteorol. Soc.* **121**, 821-851

- _____, 1995: The Evolution of Vortices in Vertical Shear. I: Large scale asymmetries, *Q. J. R. Meteorol. Soc.* **126**, 3137-3159
- Krishnamurti, T. N., 1968: A diagnostic balance model for studies of weather systems of low and high latitudes, Rossby number less than 1. *Mon. Wea. Rev.*, **96**, 197-207
- Liu, Y., D.-L. Zhang, and M. K. Yau, 1999: A multiscale numerical study of Hurricane Andrew (1992). Part II: Kinematics and inner-core structures. *Mon. Wea. Rev.*, **127**, 2597–2616
- Molinari, J., S. Skubis, D. Vollaro, F. Alsheimer, and H. E. Willoughby, 1998: Potential vorticity analysis of tropical cyclone intensification. *J. Atmos. Sci.*, **55**, 2632–2644
- Möller, J. D., and L. J. Shapiro, 2002: Balanced contributions to the intensification of Hurricane Opal as diagnosed from a GFDL model forecast. *Mon. Wea. Rev.*, **130**, 1866–1881
- _____, and S. C. Jones, 1998: Potential Vorticity Inversion for Tropical Cyclones Using the Asymmetric Balance Theory. *J. Atmos. Sci.*, **55**, 259-282
- _____, and M. T. Montgomery, 1998: Vortex Rossby Waves and Hurricane Intensification in a Barotropic Model, *J. Atmos. Sci.*, **56**, 1674-1691
- Montgomery, M. T., and J. L. Franklin, 1998: An assessment of the balance approximation in hurricanes. *J. Atmos. Sci.*, **55**, 2193–2200
- _____, and R. J. Kallenbach, 1997: A theory for vortex Rossby-waves and its application to spiral bands and intensity changes in hurricanes, *Q. J. R. Meteorol. Soc.* **123**, 435-465
- Morgan, M. C., 1999: Using Piecewise Potential Vorticity Inversion to Diagnose Frontogenesis. Part I: A Partitioning of the **Q** Vector Applied to Diagnosing Surface Frontogenesis and Vertical Motion. *Mon. Wea. Rev.* **127**, 2796-2821

- Schechter, D. A., and M. T. Montgomery, 2004: Damping and pumping of a vortex Rossby wave in a monotonic cyclone: Critical layer stirring versus inertia-buoyancy wave emission. *Phy. Of. Fluids*, **16**, 1334-1349.
- Shapiro, L. J., 1996: The motion of Hurricane Gloria: A potential vorticity diagnosis. *Mon. Wea. Rev.*, **124**, 2497–2508
- _____, and M. T. Montgomery, 1993: A three-dimensional balance theory for rapidly rotating vortices. *J. Atmos. Sci.*, **50**, 3322–3335
- _____, and J. L. Franklin, 1995: Potential vorticity in Hurricane Gloria. *Mon. Wea. Rev.*, **123**, 1465–1475
- _____, and J. L. Franklin, 1999: Potential vorticity asymmetries and tropical cyclone motion. *Mon. Wea. Rev.*, **127**, 124–131
- Wang, X.-B., D.-L. Zhang, 2003: Potential Vorticity Diagnosis of a Simulated Hurricane. Part I: Formulation and Quasi-Balanced Flow. *J. Atmos. Sci.*, **60**, 1593-1607
- Wu, C.-C., and K. A. Emanuel, 1995a: Potential vorticity diagnostics of hurricane movement. Part I: A case study of Hurricane Bob (1991). *Mon. Wea. Rev.*, **123**, 69–92
- _____, and K. A. Emanuel, 1995b: Potential vorticity diagnostics of hurricane movement. Part II: Tropical storm Ana (1991) and Hurricane Andrew (1992). *Mon. Wea. Rev.*, **123**, 93–109
- Wang, Y., and G. J. Holland, 1996: Tropical Cyclone Motion and Evolution in Vertical Shear, *J. Atmos. Sci.*, **53**, 3313–3332
- Yang Y., 2002: Vortex Rossby waves in a numerically simulated Tropical Cyclone. Part II: The Role in Tropical Cyclone Structure and Intensity Changes, *J. Atmos. Sci.*, **59**, 1239-1262

- ____, 2002: Vortex Rossby waves in a numerically simulated Tropical Cyclone. Part I: Overall Structure, Potential Vorticity, and Kinetic Energy Budgets, *J. Atmos. Sci.*, **59**, 1213-1238
- Yau, M. K., Y.-B. Liu, D.-L. Zhang, Y.-S. Chen, 2004: A Multiscale Numerical Study of Hurricane Andrew (1992). Part VI: Small-Scale Inner-Core Structures and Wind Streaks. *Mon. Wea. Rev.*: **132**, 1410–1433
- Zhang, D.-L., Y. Liu, and M. K. Yau, 2000: A multiscale numerical study of Hurricane Andrew (1992). Part III: Dynamically induced vertical motion. *Mon. Wea. Rev.*, **128**, 3772–3788
- ____, Y. Liu, and M. K. Yau, 2001: A multiscale numerical study of Hurricane Andrew (1992). Part IV: Unbalanced flows. *Mon. Wea. Rev.*, **129**, 92–107
- ____, Y. Liu, and M. K. Yau, 2002: A multiscale numerical study of Hurricane Andrew (1992). Part V: Inner-core thermodynamics. *Mon. Wea. Rev.*, **130**, 2745–2763
- ____, and C. K. Kieu, 2005: Shear-Forced Vertical Circulations in Tropical Cyclones. *Geophys. Res. Lett.*, **32**, L13822, doi:10.1029/2005GL023146
- Zhu, T., D.-L. Zhang, and F. Weng, 2004: Numerical Simulation of Hurricane Bonnie (1998). Part I: Eyewall Evolution and Intensity Changes. *Mon. Wea. Rev.*, **132**, 225–241

Figure captions

Figure 1. Time series of (a) maximum wind (ms^{-1}) at $z = 1\text{km}$, (b) surface pressure level (mb), and (c) mass-weighted Potential Vorticity (PVU unit) of a 5-day simulation of Hurricane Bonnie initialized at 0000 UTC 22 August 1998. The mass-weighted PV is an average over the volume $100\text{ km} \times 100\text{ km} \times 10\text{ km}$ (bold solid line), $50\text{ km} \times 50\text{ km} \times 10\text{ km}$ (light solid line), and $25\text{ km} \times 25\text{ km} \times 10\text{ km}$ (dashed line)

Figure 2. The total PV distribution (PVU unit) at $z = 3\text{ km}$ from a 50 h-simulation of Hurricane Bonnie during its maximum stage at (a) 0200 UTC, (b) 0245 UTC, and (c) 0330 UTC on 24 August 1998. Superimposed is the heating distribution (contours at 30 K/h for positive value and 10 K/h for negative value). Bold letter A indicates the trace of the movement of PV

Figure 3. (a) An area-averaged (storm-relative) hodograph over an area of $576\text{ km} \times 576\text{ km}$ centered in the eye, which are obtained at 0000 UTC 24 August 1998, and (b) cross sections through the storm center along the shear vector of (storm-relative) in-plane flow vectors and the vertical motion forced by the dry dynamical processes (every 0.2 m s^{-1}), which are obtained at 0000 UTC 24 August 1998. Solid (dotted) lines are for upward (downward) motion. Note that the vertical motion vectors have been amplified by a factor of 5.

Figure 4. The same as Fig. 2 but for the radar reflectivity (dBz) at $z = 5\text{km}$. Superimposed is vertical motion (contoured at 1 ms^{-1})

Figure 5. The distribution of PV valid at the maximum stage of Bonnie (0245 UTC 24 August 1998) for (a) West-East vertical cross section taken as an average of four slices through the center, and (b) the height-azimuth cross section averaged within the eyewall. All

are superimposed by the wind flow vectors. Note that vertical velocity have been amplified by a factor of 5.

Figure 6. The same as Fig 5 but for the distribution of PV anomaly. The bold gray circle in panel (a) represents the partitioning of total PV anomaly into four pieces used in this study. The positive PV anomaly (red shading) between the bold solid line at the lower right corner and the bold gray dash line represents piece P1, and negative PV anomaly between the bold gray dash line and the bold solid line at the top left corner represents piece P2. Letter A corresponds to that in Fig. 5b

Figure 7. Total PV distribution (shaded) in PVU unit superimposed with the wind fields at $z = 3$ km from the 88h-simulation of Hurricane Bonnie during its eyewall replacement stage at (a) 1615 UTC, (b) 1700 UTC, and (c) 1745 UTC on 25 August 1998. The bold grey closed curve in panel b represents a portion of PV which will be inverted

Figure 8. The same as Fig.3 but for (a) 0015 UTC, (b) 0100 UTC, and (c) 0145 UTC on 26 August 1998. Note the domain size is 180 km x 180 km instead of 100 km x 100 km as in Fig. 3 because the outer eyewall during the eyewall replacement process is as large as 120 km.

Figure 9. West-East vertical cross sections of PV (shading in PVU unit) superimposed by the in-plane secondary circulation for (a) 1700 UTC August 2 corresponding to Fig. 7b, and (b) 0100 UTC August 26 1998 corresponding to Fig. 8b . Note that vertical motion has been multiplied by a factor of 10 to enhance the double eyewall.

Figure. 10. The perturbation fields (contours) associated with positive PV anomaly (shaded) at the outer eyewall valid at 1630 UTC 25 August 1998 for (a) pressure perturbation at intervals of 1 hPa at $z = 3$ km, (b) potential temperature at intervals of 0.3 K at $z = 3$ km, and

(c) vertical motion at intervals of $5 \times 10^{-2} \text{ ms}^{-1}$ at $z = 1 \text{ km}$. Panels (a) and (b) are superimposed by the rotational wind field induced by the corresponding PV anomaly, while (c) is superimposed by the divergent wind. Shadings denote the PV anomaly piece (PVU unit). Solid (dash) lines are for positive (negative) values. The bold gray dot-dash circle represents the inner radius at the corresponding levels.

Figure. 11. The same as Fig. 10 but for $z = 10 \text{ km}$. Note that the contours in panel 11a are at 0.3 hPa intervals for the purpose of presentation

Figure. 12. East-West vertical cross sections of perturbation fields (contours) superimposed with in-plane flow vectors associated with the PV anomaly (shaded) at the outer eyewall valid at 1630 UTC 25 August 1998 for (a) pressure perturbation at intervals of 0.5 hPa, (b) potential temperature perturbation at intervals of 0.3 K at $z = 3 \text{ km}$ Shadings denote the PV anomaly piece (in PVU unit). Solid (dash) lines are for positive (negative) values. Note the scale of vector is in unit of 10^{-1} ms^{-1}

Figure. A1. (a) Distribution of eddy term $\left(\frac{1}{r} \frac{\partial \{r \overline{(u'q')}\}}{\partial r}\right)$ with radius (in unit of $10^{-5} \text{ PVU} \times \text{s}^{-1}$) due to wave activities obtained by temporally averaging 24 datasets at 15-min intervals during the 6-h period from the 36 – 48 h simulation ending 0000 UTC 24 August 1998 and mass weighted from surface to 5 km. The abscissa is radius in km, and the ordinate is in unit of $1 \times 10^{-9} \text{ s}^{-2}$, (b) distribution of the same eddy term with azimuthal angle averaged over 24 data sets at $z = 3 \text{ km}$ within the eyewall (c) distribution of eddy flux term $(u'q')$ (in $\text{ms}^{-1} \times \text{PVU}$ unit) with azimuthal angle averaged over 24 data sets at $z = 3 \text{ km}$ during the same period as in panel a.

Figure. A2. The difference between the sum of pressure perturbations associated with four PV anomaly pieces and the pressure perturbation associated with the sum of four pieces of

PV anomalies at 0000 UTC 24 August 1998 (contoured at interval of 0.1 hPa) for (a) $z = 10$ km, (b) $z = 5$ km, and (c) $z = 1$ km

Figure A3. The same as Fig. 10 but for perturbation potential temperature

Figure A4. The total PV distribution (PVU unit) at $z = 5$ km from a 50 h-simulation of Hurricane Bonnie during its maximum stage at (a) 0200 UTC, (b) 0245 UTC, and (c) 0330 UTC on 24 August 1998. Superimposed is the heating distribution (contours at 30 K/h for positive value and 10 K/h for negative value). Bold letter A indicates the trace of the movement of PV.

Figure A5. The same as Fig. 2 but for the distribution of PV anomaly. The anomaly is computed by subtracting the azimuthally averaged PV from the total. Superimposed is the perturbation flow field. Letter A is the trace of positive PV anomaly corresponding exactly to that in Fig. 2. The bold gray circles represent the eyewall.

Figure A6. The pressure perturbation field (contour) associated with piece P1 valid at 0245 UTC 24 August 1998 of Hurricane Bonnie for (a) $z = 10$ km at intervals of 0.1 hPa, (b) $z = 5$ km at intervals of 0.3 hPa, and (c) $z = 1$ km at intervals of 0.3 hPa. All are superimposed by the wind field induced by the corresponding PV anomaly. Shadings denote the PV anomaly piece P1 (PVU unit). Solid (dash) lines are for positive (negative) values. The bold gray dot-dash circle is the radius of maximum wind at the corresponding level.

Figure A7. The potential temperature perturbation field (contours at intervals of 0.5 K) associated with piece P1 valid at 0245 UTC 24 August 1998 of Hurricane Bonnie for (a) $z = 10$ km, (b) $z = 5$ km, and (c) $z = 1$ km. All are superimposed by the wind field induced by the corresponding PV anomaly. Shadings denote the PV anomaly piece P1. Solid (dash) lines are for positive (negative) values

Figure A8. East-West vertical cross section through the center of Bonnie associated with piece P1 valid at 0245 UTC 24 August 1998 for (a) pressure perturbation at intervals of 0.3 hPa, (b) potential temperature perturbation at intervals of 0.5 K, and (c) y-component of wind field at intervals of 1 ms^{-1} . Shadings denote the PV anomaly piece P1. Solid (dash) lines are for positive (negative) values

Figure A9. The pressure perturbation field (contour) associated with piece P2 for (a) $z = 10$ km at intervals of 0.1 hPa, (b) $z = 5$ km at intervals of 0.3 hPa, and (c) $z = 1$ km at intervals of 0.3 hPa.

Figure A10. The potential temperature perturbation field (contours at intervals of 0.5 K) associated with piece P2 for (a) $z = 10$ km, (b) $z = 5$ km, and (c) $z = 1$ km. All are superimposed by the wind field induced by the corresponding PV anomaly.

Figure. A12. East-West vertical cross section through the center of Bonnie associated with piece P2 for (a) pressure perturbation at intervals of 0.3 hPa, (b) potential temperature perturbation at intervals of 0.5 K, and (c) y-component of wind field at intervals of 1 ms^{-1} .

Figure. A13. The pressure perturbation field (contour) associated with piece P3 for (a) $z = 10$ km at intervals of 0.1 hPa, (b) $z = 5$ km at intervals of 0.3 hPa, and (c) $z = 1$ km at intervals of 0.3 hPa.

Figure. A13. The potential temperature perturbation field (contours at intervals of 0.5 K) associated with piece P3 for (a) $z = 10$ km, (b) $z = 5$ km, and (c) $z = 1$ km. All are superimposed by the wind field induced by the corresponding PV anomaly.

Figure. A14. East-West vertical cross section through the center of Bonnie associated with piece P3 for (a) pressure perturbation at intervals of 0.3 hPa, (b) potential temperature perturbation at intervals of 0.5 K, and (c) y-component of wind field at intervals of 1 ms^{-1} .

Figure. A15. The sum of pressure perturbations (contoured at intervals of 1 hPa) associated with pieces P1, P2, P3, P4 valid at 0245 UTC 24 August 1998 of Hurricane Bonnie for (a) $z = 10$ km, (b) $z = 5$ km, and (c) $z = 1$ km. All are superimposed by the wind field induced by the all PV anomalies. Shadings denote the total PV anomaly. Solid (dash) lines are for positive (negative) values

Figure. A16. The sum of potential temperature perturbations (contoured at intervals of 1 K) associated with pieces P1, P2, P3, P4 for (a) $z = 1$ km, (b) $z = 5$ km, and (c) $z = 10$ km. Solid (dash) lines are for positive (negative) values

Figures

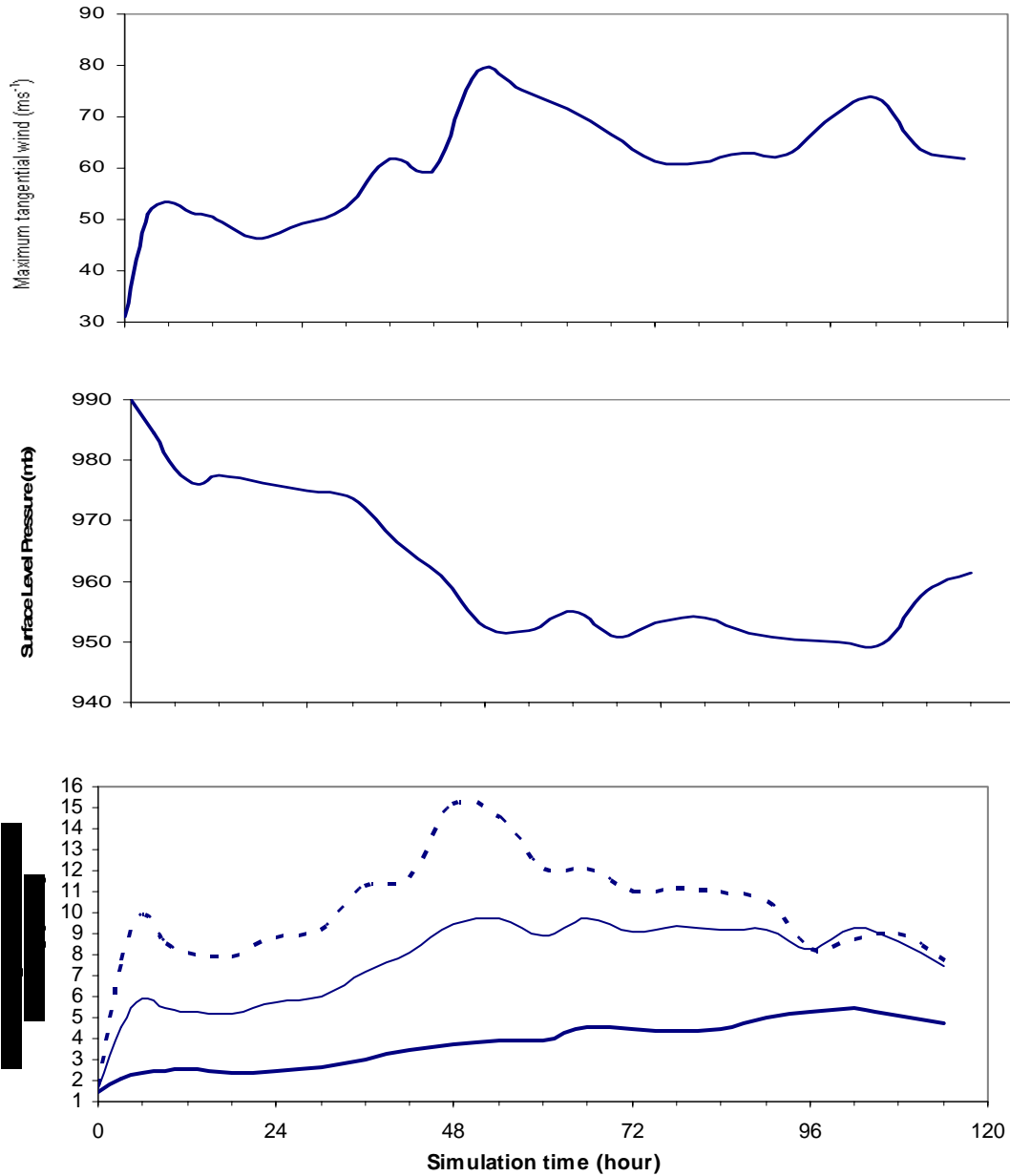


Figure 1. Time series of (a) maximum wind (ms^{-1}) at $z = 1\text{km}$, (b) surface pressure level (mb), and (c) mass-weighted Potential Vorticity (PVU unit) of a 5-day simulation of Hurricane Bonnie initialized at 0000 UTC 22 August 1998. The mass-weighted PV is an average over the volume 100 km x 100 km x 10 km (bold solid line), 50 km x 50 km x 10 km (light solid line), and 25 km x 25 km x 10 km (dashed line)

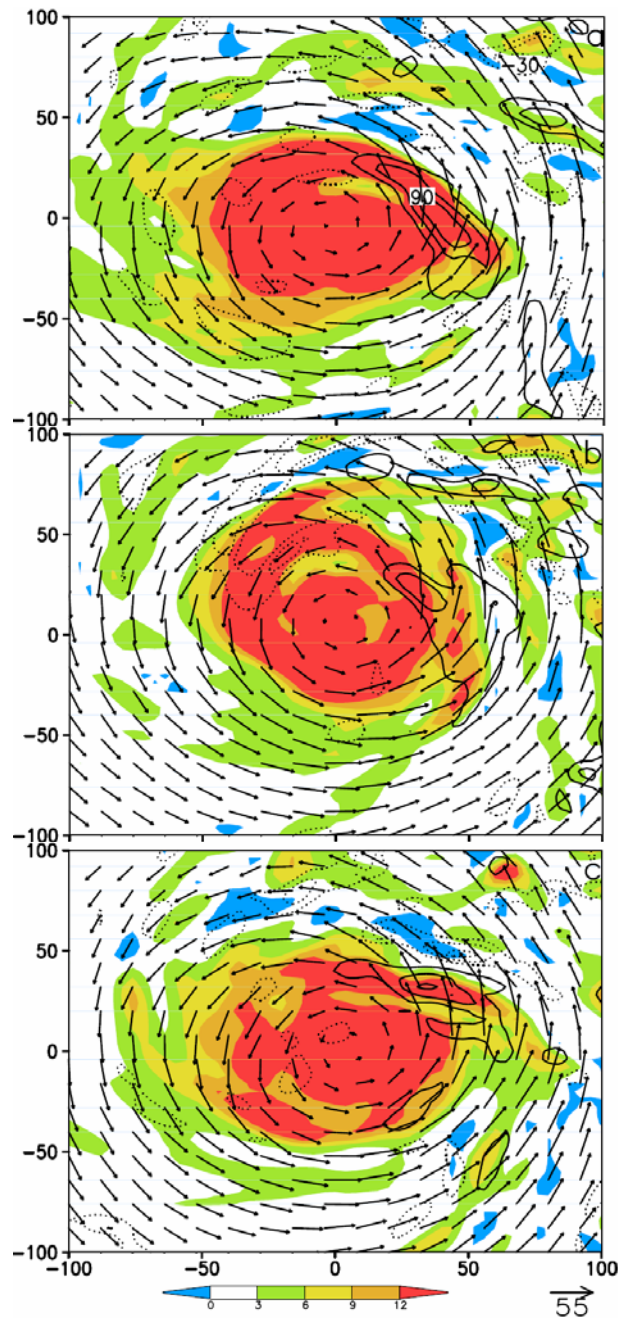


Figure 2. The total PV distribution (PVU unit) at $z = 3$ km from a 50 h-simulation of Hurricane Bonnie during its maximum stage at (a) 0200 UTC, (b) 0245 UTC, and (c) 0330 UTC on 24 August 1998. Superimposed is the heating distribution (contours at 30 K/h for positive value and 10 K/h for negative value). Bold letter A indicates the trace of the movement of PV.

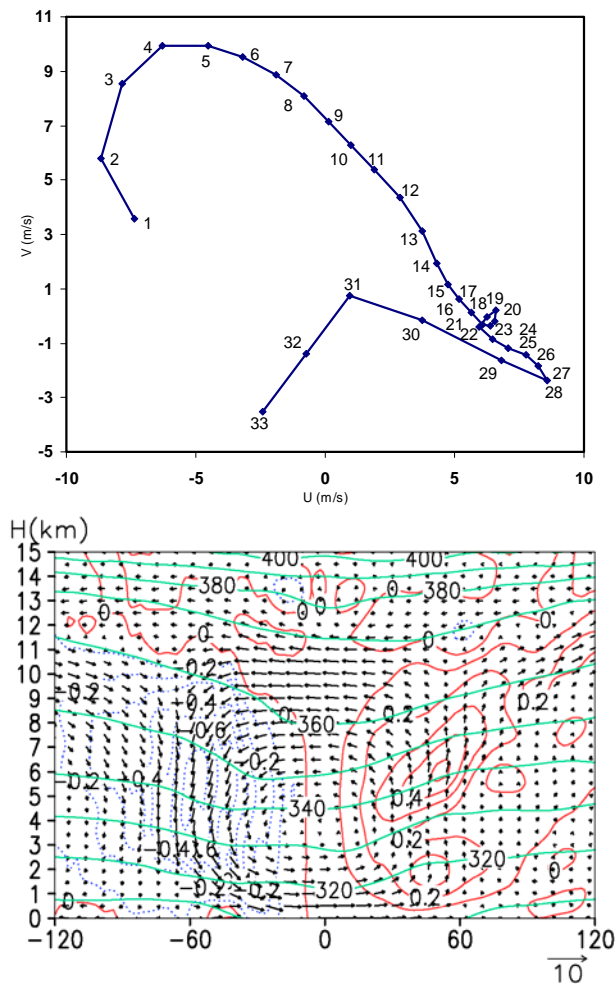


Figure 3. (a) An area-averaged (storm-relative) hodograph over an area of 576 km x 576 km centered in the eye, which are obtained at 0000 UTC 24 August 1998, and (b) cross sections through the storm center along the shear vector of (storm-relative) in-plane flow vectors and the vertical motion forced by the dry dynamical processes (every 0.2 m s^{-1}), which are obtained at 0000 UTC 24 August 1998. Solid (dotted) lines are for upward (downward) motion. Note that the vertical motion vectors have been amplified by a factor of 5.

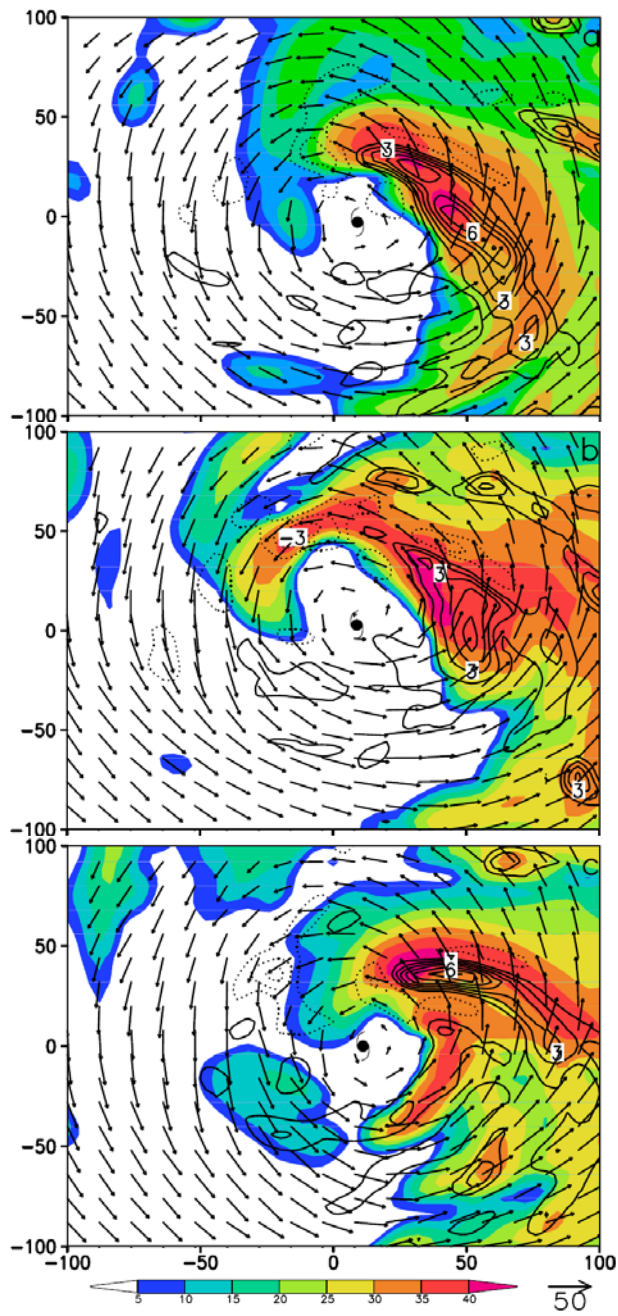


Figure 4. The same as Fig. 2 but for the radar reflectivity (dBZ) at $z = 5\text{km}$. Superimposed is vertical motion (contoured at 1 ms^{-1})

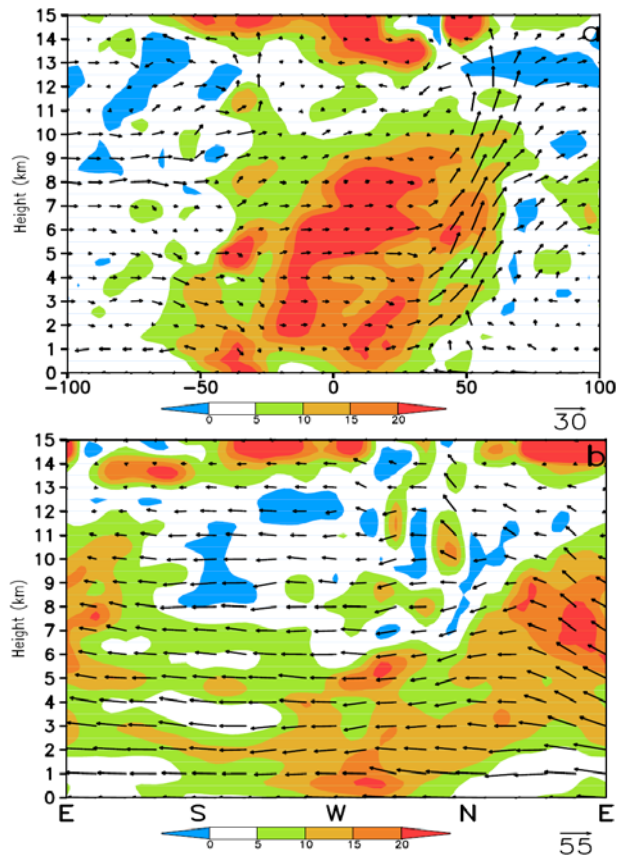


Figure 5. The distribution of PV valid at the maximum stage of Bonnie (0245 UTC 24 August 1998) for (a) West-East vertical cross section taken as an average of four slices through the center, and (b) the height-azimuth cross section averaged within the eyewall. All are superimposed by the wind flow vectors. Note that vertical velocity have been amplified by a factor of 5.

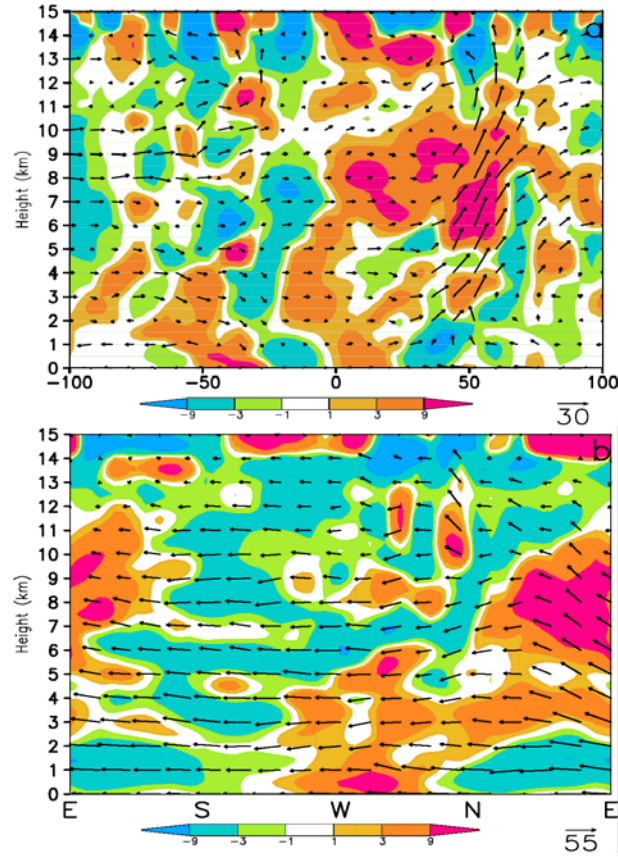


Figure 6. The same as Fig 5 but for the distribution of PV anomaly. The bold gray circle in panel (a) represents the partitioning of total PV anomaly into four pieces used in this study. The positive PV anomaly (red shading) between the bold solid line at the lower right corner and the bold gray dash line represents piece P1, and negative PV anomaly between the bold gray dash line and the bold solid line at the top left corner represents piece P2. Letter A

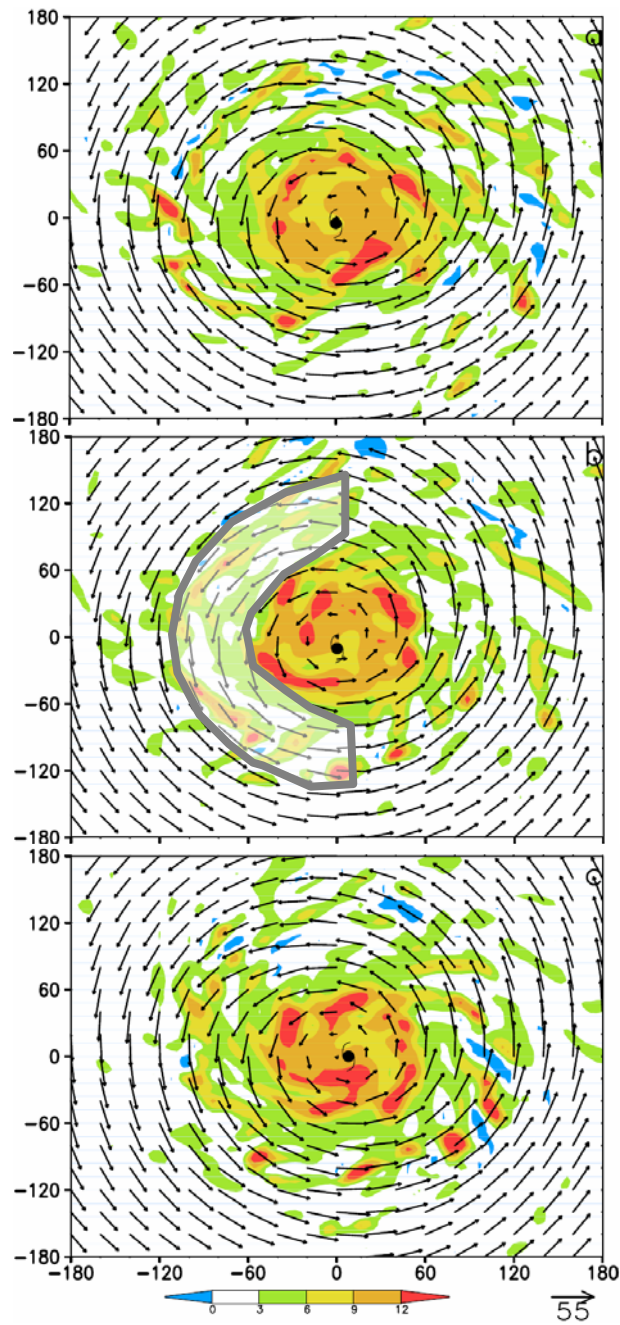


Figure 7. Total PV distribution (shaded) in PVU unit superimposed with the wind fields at $z = 3$ km from the 88h-simulation of Hurricane Bonnie during its eyewall replacement stage at (a) 1615 UTC, (b) 1700 UTC, and (c) 1745 UTC on 25 August 1998. The bold grey closed curve in panel b represents a portion of PV which will be inverted

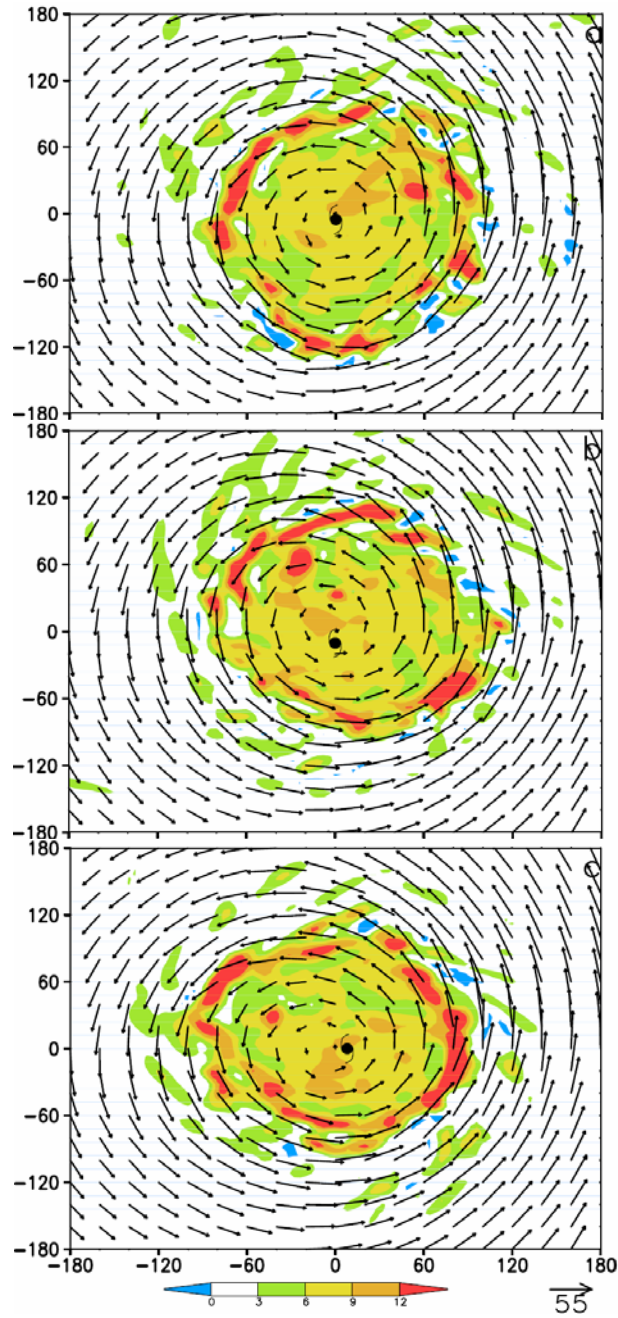


Figure 8. The same as Fig.3 but for (a) 0015 UTC, (b) 0100 UTC, and (c) 0145 UTC on 26 August 1998. Note the domain size is 180 km x 180 km instead of 100 km x 100 km as in Fig. 3 because the outer eyewall during the eyewall replacement process is as large as 120 km.

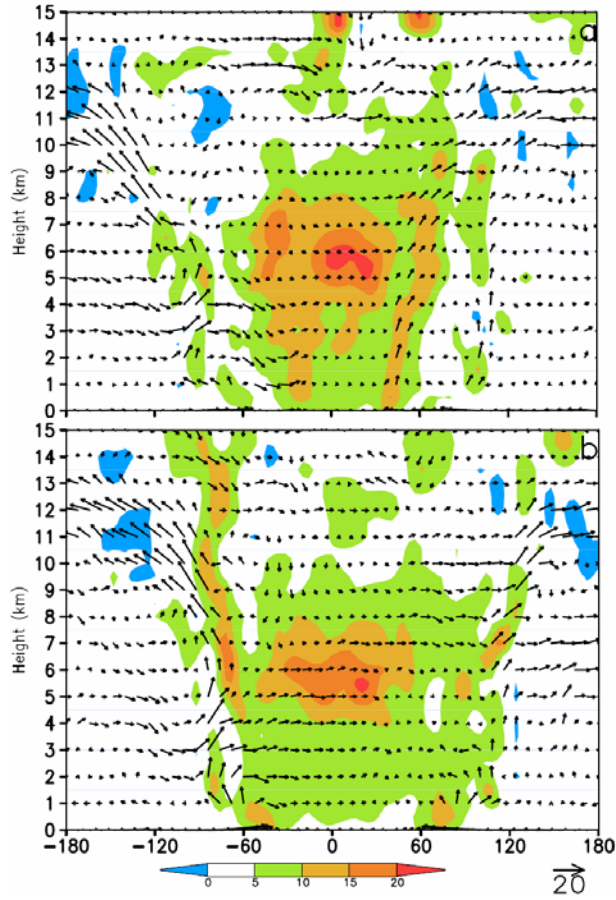


Figure 9. West-East vertical cross sections of PV (shading in PVU unit) superimposed by the in-plane secondary circulation for (a) 1700 UTC August 2 corresponding to Fig. 7b, and (b) 0100 UTC August 26 1998 corresponding to Fig. 8b . Note that vertical motion has been multiplied by a factor of 10 to enhance the double eyewall.

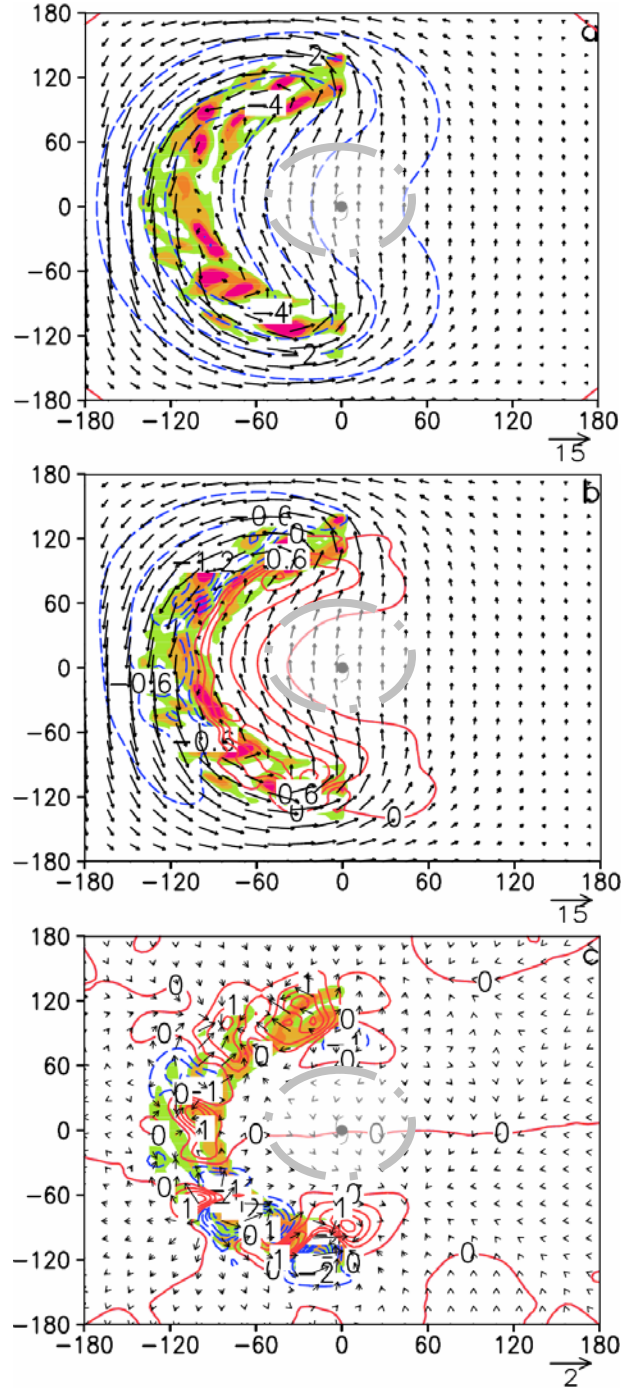


Figure. 10. The perturbation fields (contours) associated with positive PV anomaly (shaded) at the outer eyewall valid at 1630 UTC 25 August 1998 for (a) pressure perturbation at intervals of 1 hPa at $z = 3$ km, (b) potential temperature at intervals of 0.3 K at $z = 3$ km, and (c) vertical motion at intervals of $5 \times 10^{-2} \text{ ms}^{-1}$ at $z = 1$ km. Panels (a) and (b) are superimposed by the rotational wind field induced by the corresponding PV anomaly, while (c) is superimposed by the divergent wind. Shadings denote the PV anomaly piece (PVU unit). Solid (dash) lines are for positive (negative) values. The bold gray dot-dash circle represents the inner radius at the corresponding levels.

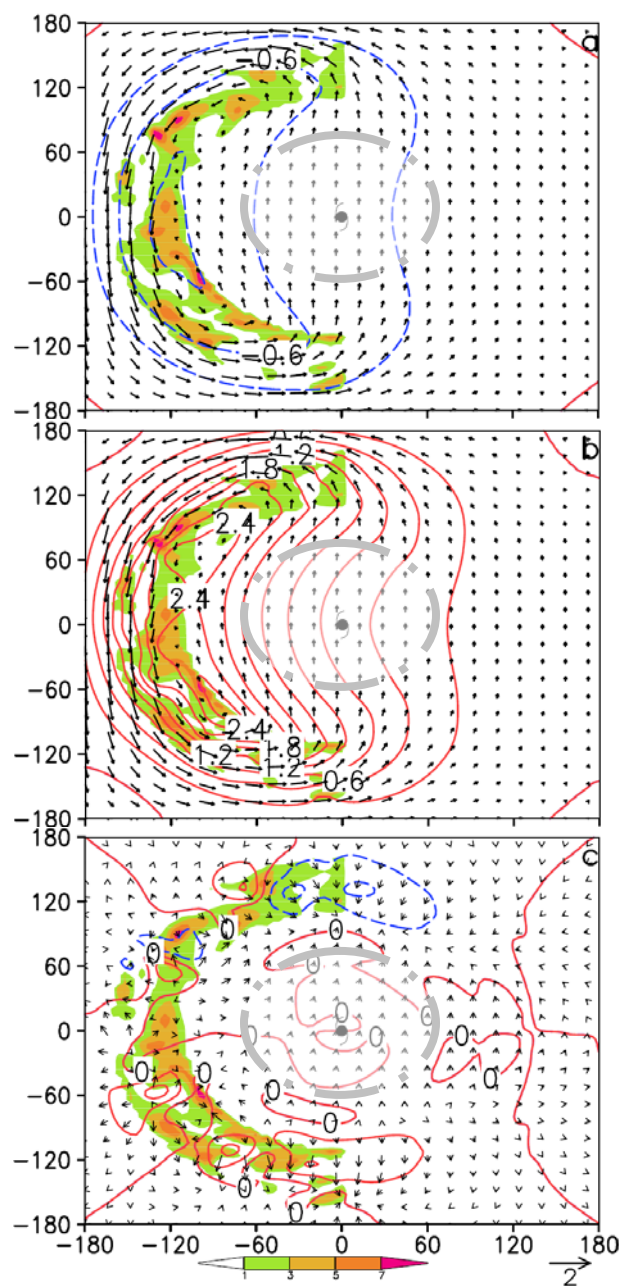


Figure. 11. The same as Fig. 10 but for $z = 10$ km. Note that the contours in panel 11a are at 0.3 hPa intervals for the purpose of presentation

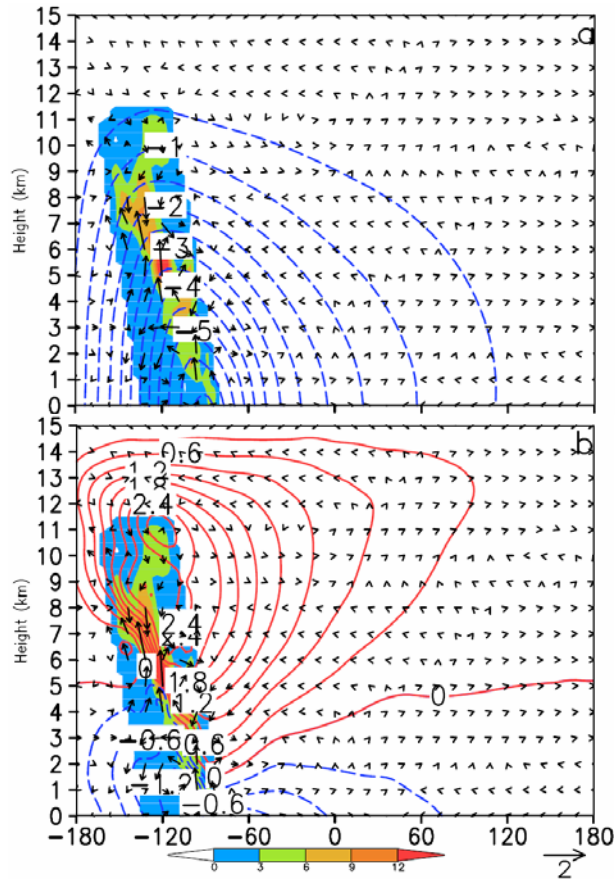


Figure. 12. East-West vertical cross sections of perturbation fields (contours) superimposed with in-plane flow vectors associated with the PV anomaly (shaded) at the outer eyewall valid at 1630 UTC 25 August 1998 for (a) pressure perturbation at intervals of 0.5 hPa, (b) potential temperature perturbation at intervals of 0.3 K at $z = 3$ km. Shadings denote the PV anomaly piece (in PVU unit). Solid (dash) lines are for positive (negative) values. Note the scale of vector is in unit of 10^{-1} ms^{-1} .

Figure Appendix

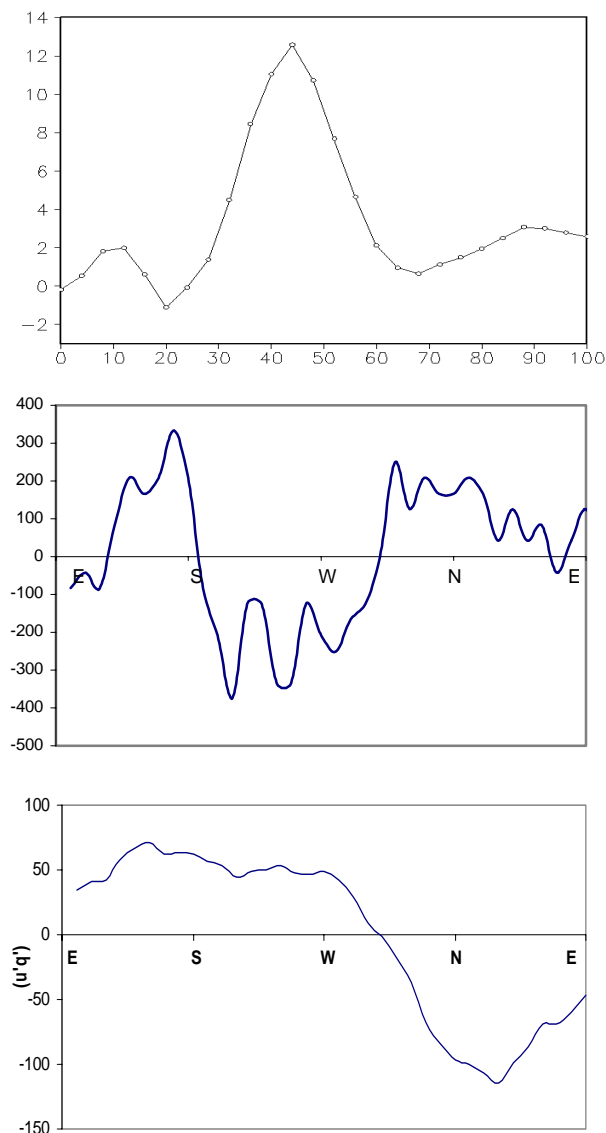


Figure. A1. (a) Distribution of eddy term $\left(\frac{1}{r} \frac{\partial \{r(u'q')\}}{\partial r}\right)$ with radius (in unit of 10^{-5} PVU \times s^{-1}) due to wave activities obtained by temporally averaging 24 datasets at 15-min intervals during the 6-h period from the 36 – 48 h simulation ending 0000 UTC 24 August 1998 and mass weighted from surface to 5 km. The abscissa is radius in km, and the ordinate is in unit of 1×10^{-9} s^{-2} , (b) distribution of the same eddy term with azimuthal angle averaged over 24 data sets at $z = 3$ km within the eyewall (c) distribution of eddy flux term $(u'q')$ (in $ms^{-1} \times$ PVU unit) with azimuthal angle averaged over 24 data sets at $z = 3$ km during the same period as in panel a.

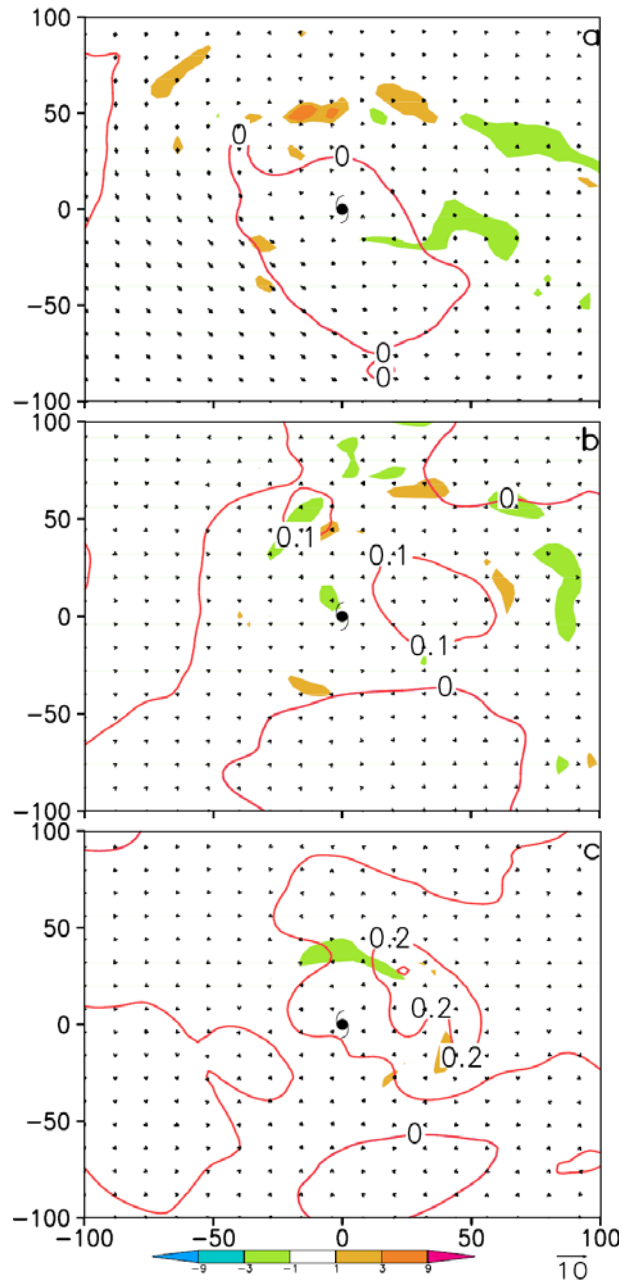


Figure. A2. The difference between the sum of pressure perturbations associated with four PV anomaly pieces and the pressure perturbation associated with the sum of four pieces of PV anomalies at 0000 UTC 24 August 1998 (contoured at interval of 0.1 hPa) for (a) $z = 10$ km, (b) $z = 5$ km, and (c) $z = 1$ km

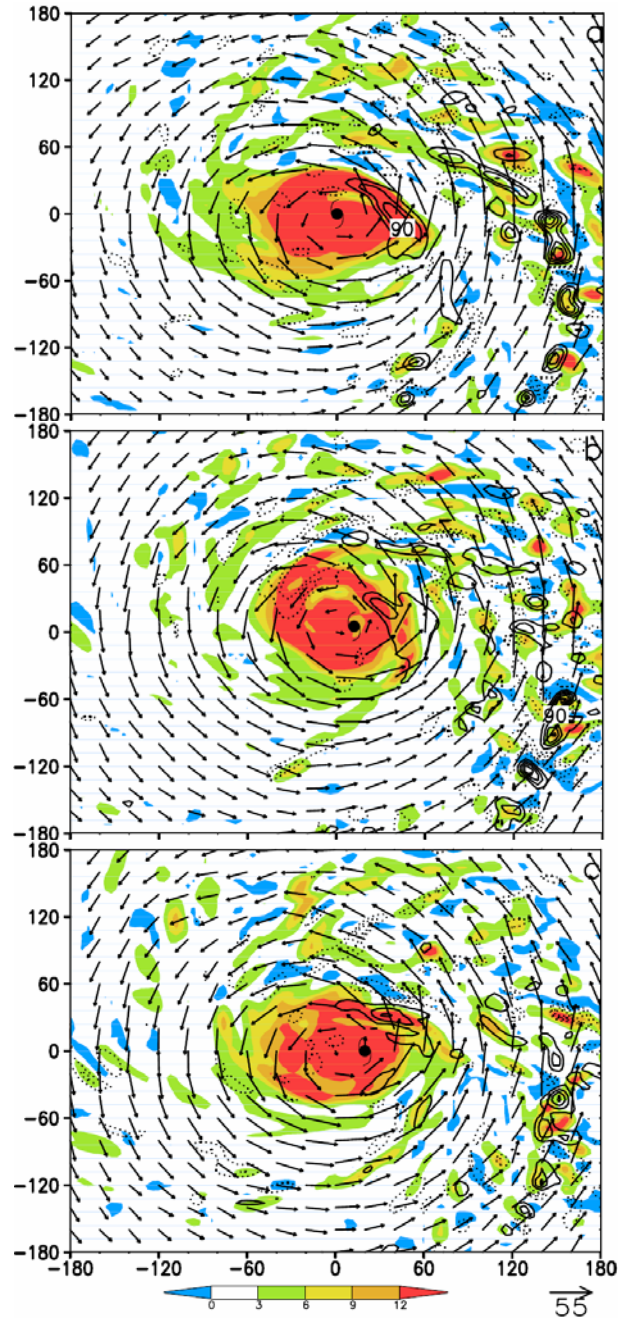


Figure A4. The total PV distribution (PVU unit) at $z = 5$ km from a 50 h-simulation of Hurricane Bonnie during its maximum stage at (a) 0200 UTC, (b) 0245 UTC, and (c) 0330 UTC on 24 August 1998. Superimposed is the heating distribution (contours at 30 K/h for positive value and 10 K/h for negative value). Bold letter A indicates the trace of the movement of PV.

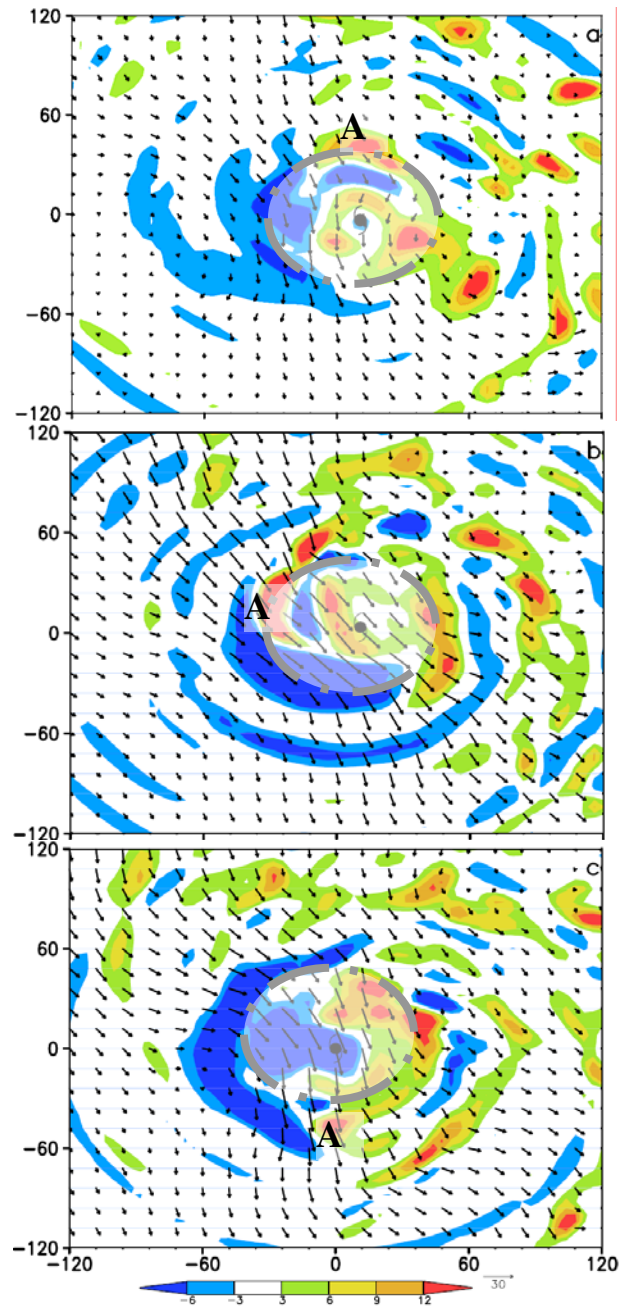


Figure A5. The same as Fig. 2 but for the distribution of PV anomaly. The anomaly is computed by subtracting the azimuthally averaged PV from the total. Superimposed is the perturbation flow field. Letter A is the trace of positive PV anomaly corresponding exactly to that in Fig. 2. The bold gray circles represent the eyewall.

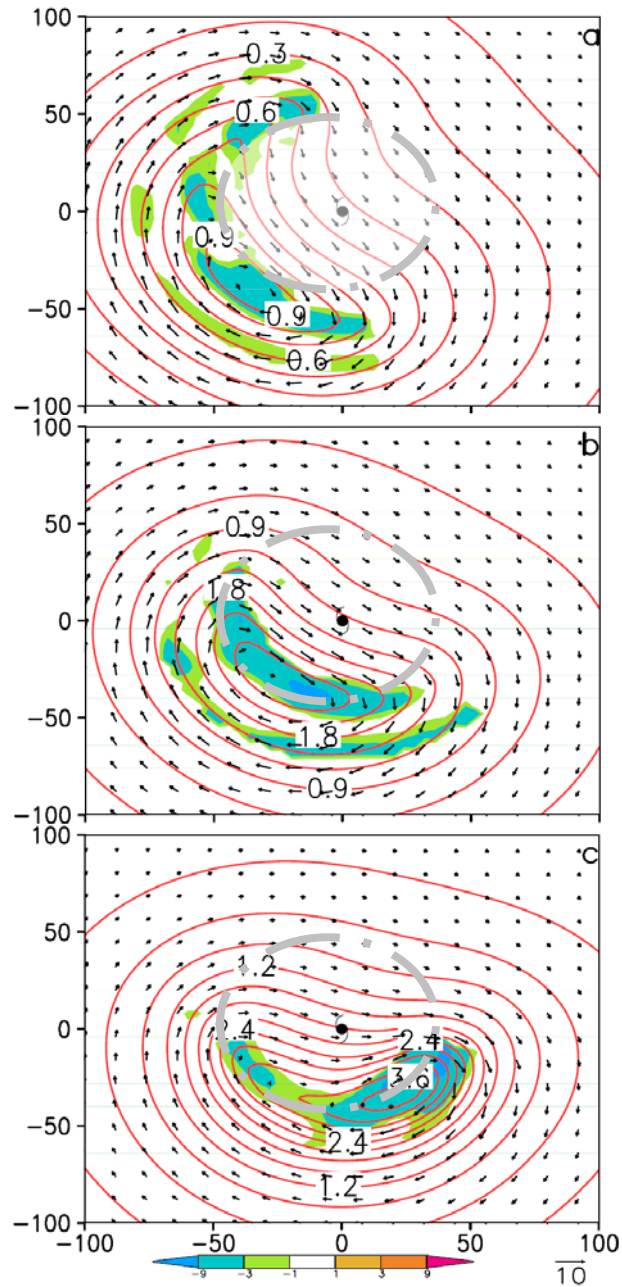


Figure A6. The pressure perturbation field (contour) associated with piece P1 valid at 0245 UTC 24 August 1998 of Hurricane Bonnie for (a) $z = 10$ km at intervals of 0.1 hPa, (b) $z = 5$ km at intervals of 0.3 hPa, and (c) $z = 1$ km at intervals of 0.3 hPa. All are superimposed by the wind field induced by the corresponding PV anomaly. Shadings denote the PV anomaly piece P1 (PVU unit). Solid (dash) lines are for positive (negative) values. The bold gray dot-dash circle is the radius of maximum wind at the corresponding level.

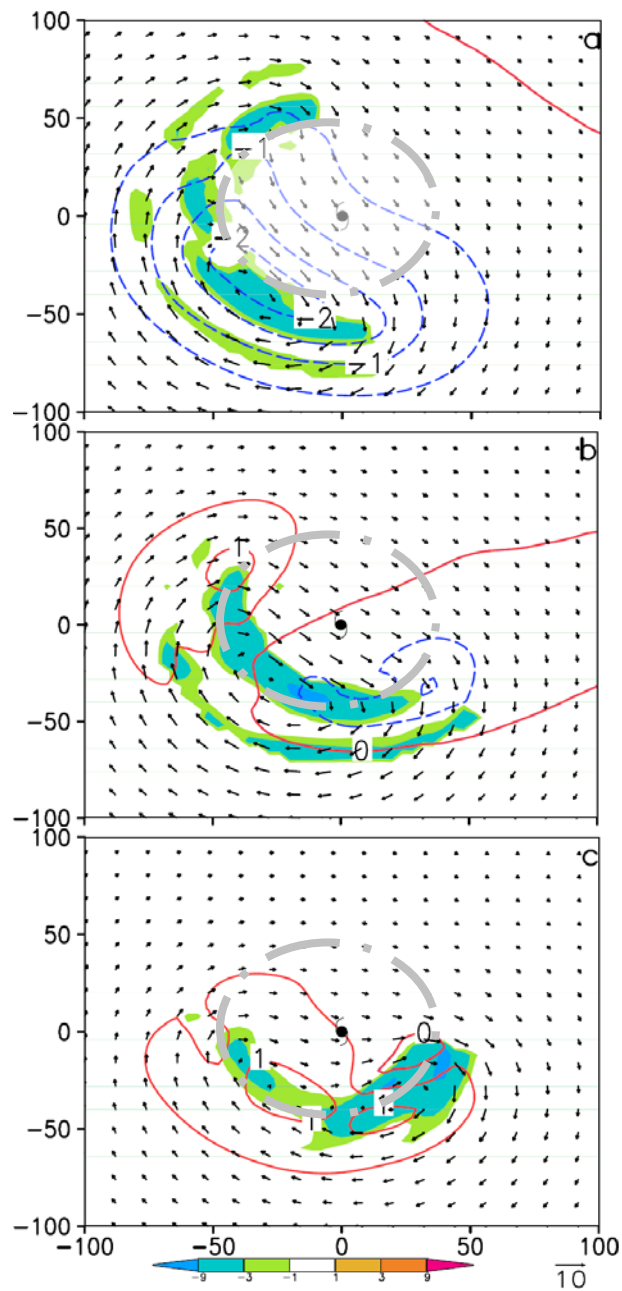


Figure A7. The potential temperature perturbation field (contours at intervals of 0.5 K) associated with piece P1 valid at 0245 UTC 24 August 1998 of Hurricane Bonnie for (a) $z = 10$ km, (b) $z = 5$ km, and (c) $z = 1$ km. All are superimposed by the wind field induced by the corresponding PV anomaly. Shadings denote the PV anomaly piece P1. Solid (dash) lines are for positive (negative) values

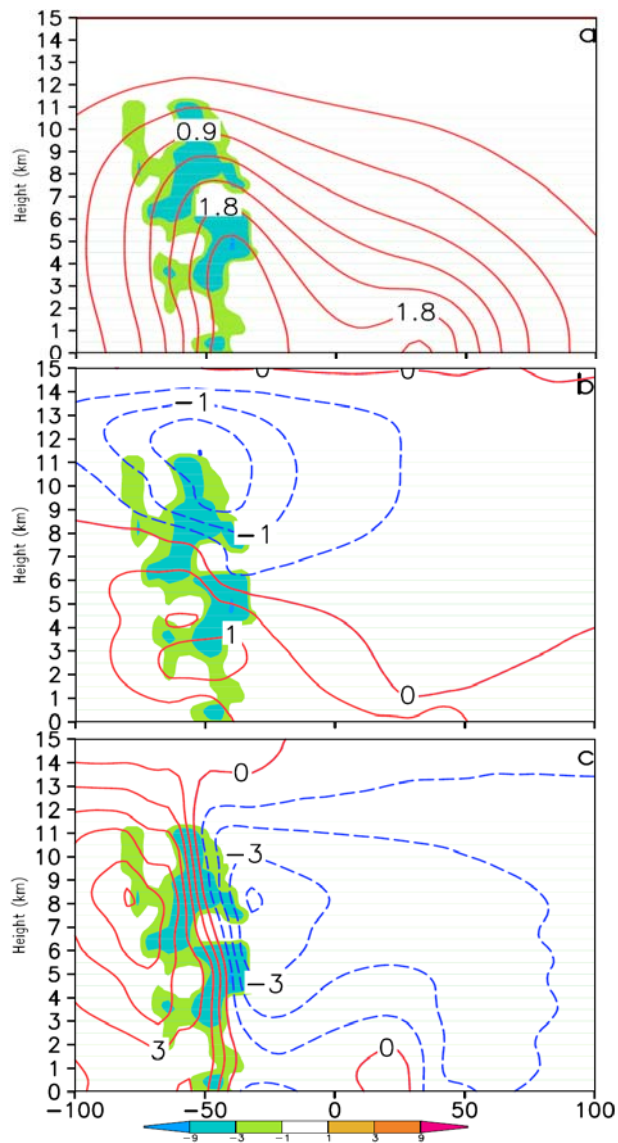


Figure A8. East-West vertical cross section through the center of Bonnie associated with piece P1 valid at 0245 UTC 24 August 1998 for (a) pressure perturbation at intervals of 0.3 hPa, (b) potential temperature perturbation at intervals of 0.5 K, and (c) y-component of wind field at intervals of 1 ms^{-1} . Shadings denote the PV anomaly piece P1. Solid (dash) lines are for positive (negative) values

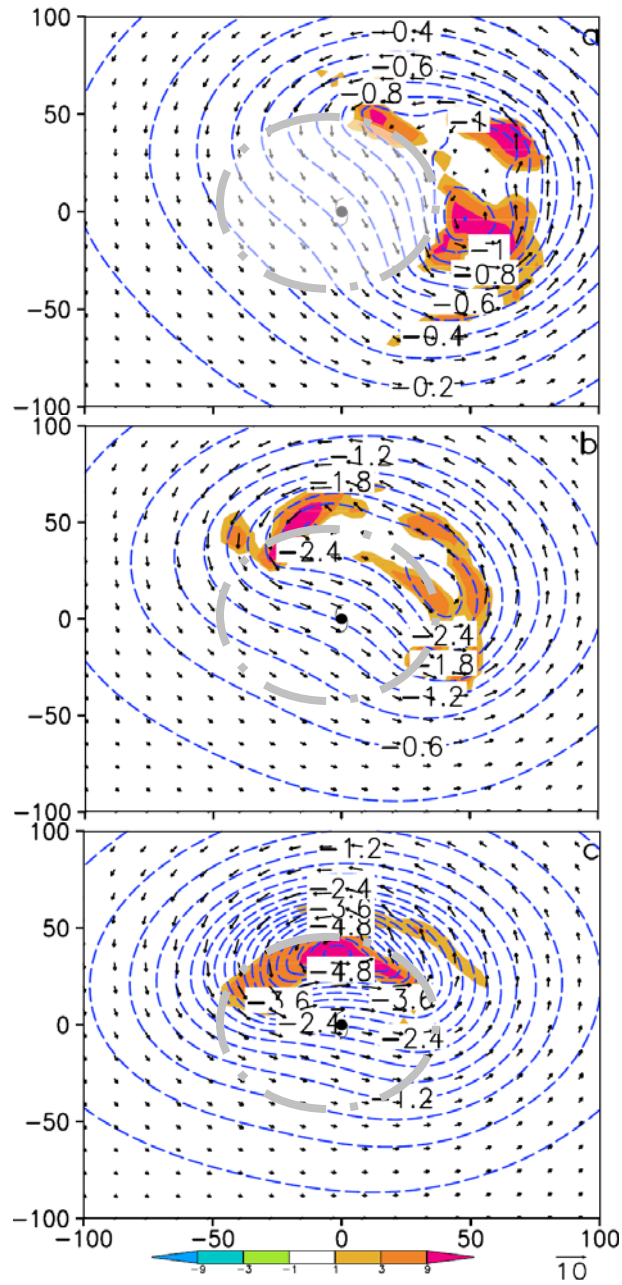


Figure A9. The pressure perturbation field (contour) associated with piece P2 for (a) $z = 10$ km at intervals of 0.1 hPa, (b) $z = 5$ km at intervals of 0.3 hPa, and (c) $z = 1$ km at intervals of 0.3 hPa.

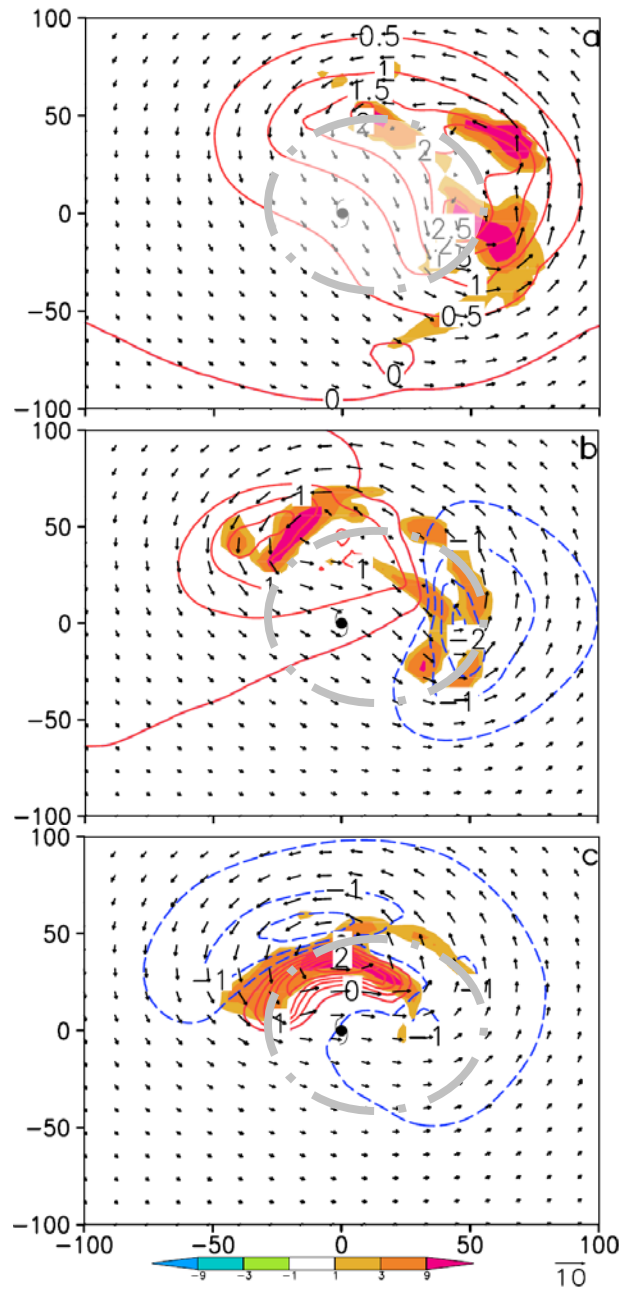


Figure A10. The potential temperature perturbation field (contours at intervals of 0.5 K) associated with piece P2 for (a) $z = 10$ km, (b) $z = 5$ km, and (c) $z = 1$ km. All are superimposed by the wind field induced by the corresponding PV anomaly.

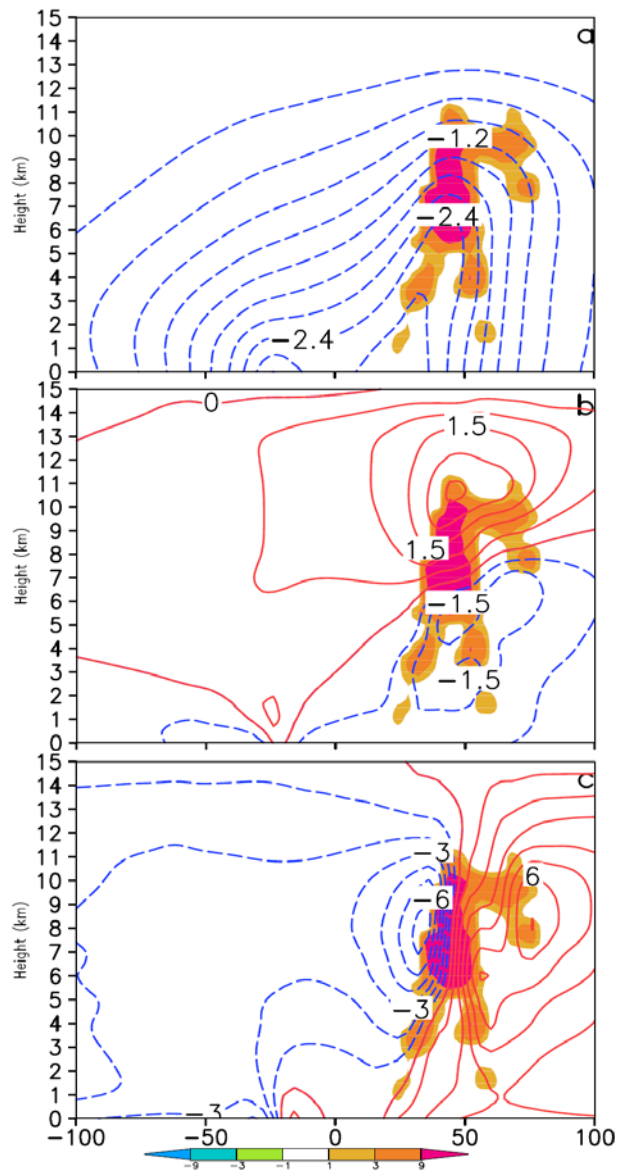


Figure. A11. East-West vertical cross section through the center of Bonnie associated with piece P2 for (a) pressure perturbation at intervals of 0.3 hPa, (b) potential temperature perturbation at intervals of 0.5 K, and (c) y-component of wind field at intervals of 1 ms^{-1} .

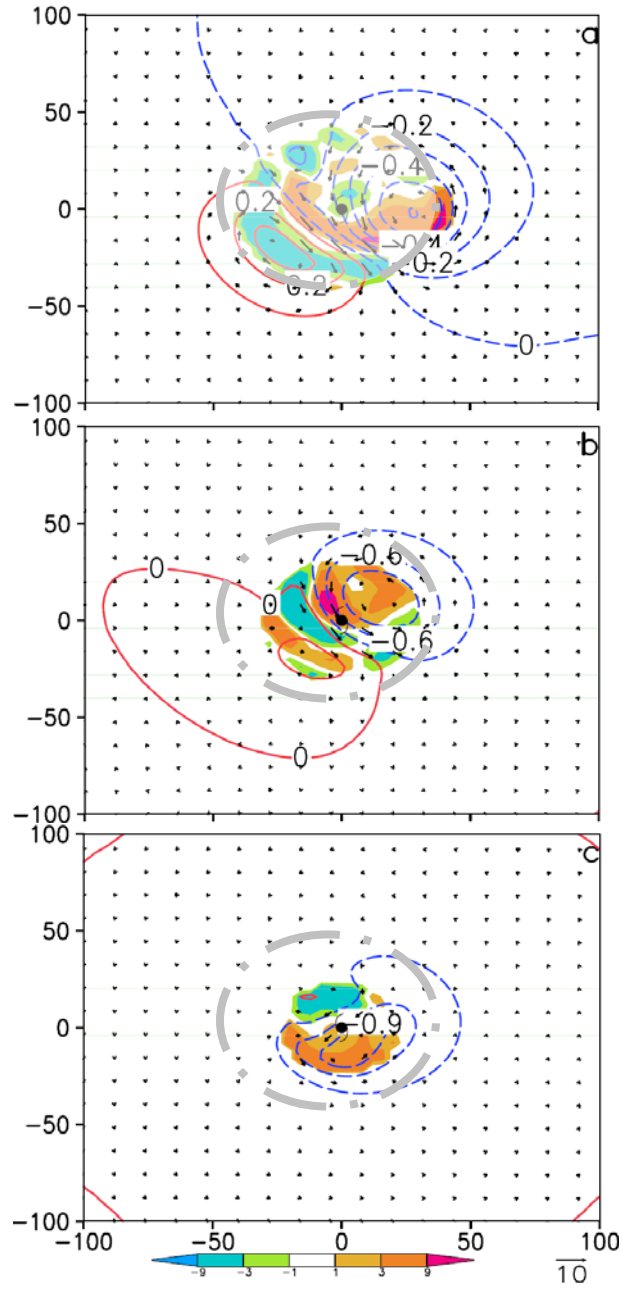


Figure. A12. The pressure perturbation field (contour) associated with piece P3 for (a) $z = 10$ km at intervals of 0.1 hPa, (b) $z = 5$ km at intervals of 0.3 hPa, and (c) $z = 1$ km at intervals of 0.3 hPa.

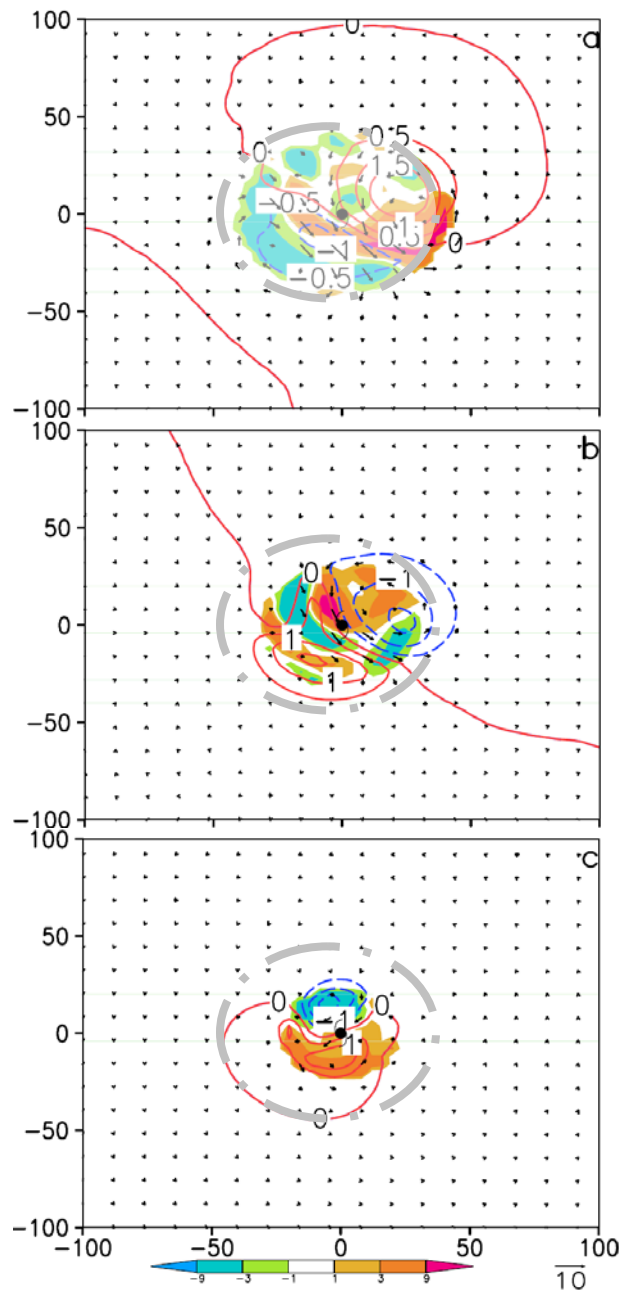


Figure. A13. The potential temperature perturbation field (contours at intervals of 0.5 K) associated with piece P3 for (a) $z = 10$ km, (b) $z = 5$ km, and (c) $z = 1$ km. All are superimposed by the wind field induced by the corresponding PV anomaly.

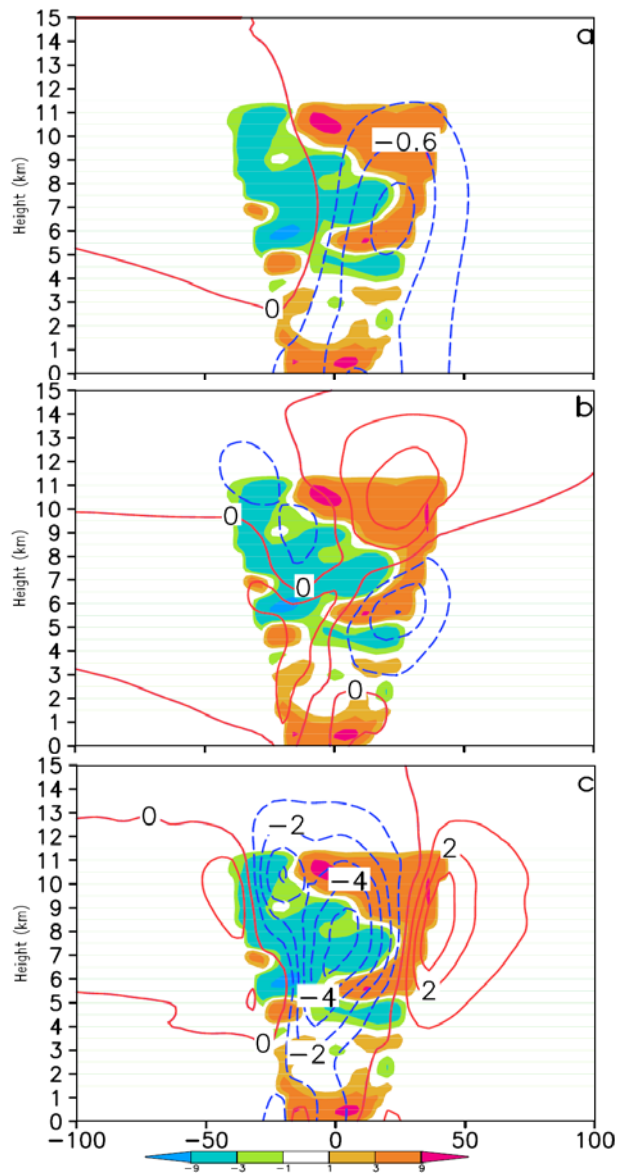


Figure. A14. East-West vertical cross section through the center of Bonnie associated with piece P3 for (a) pressure perturbation at intervals of 0.3 hPa, (b) potential temperature perturbation at intervals of 0.5 K, and (c) y-component of wind field at intervals of 1 ms⁻¹.

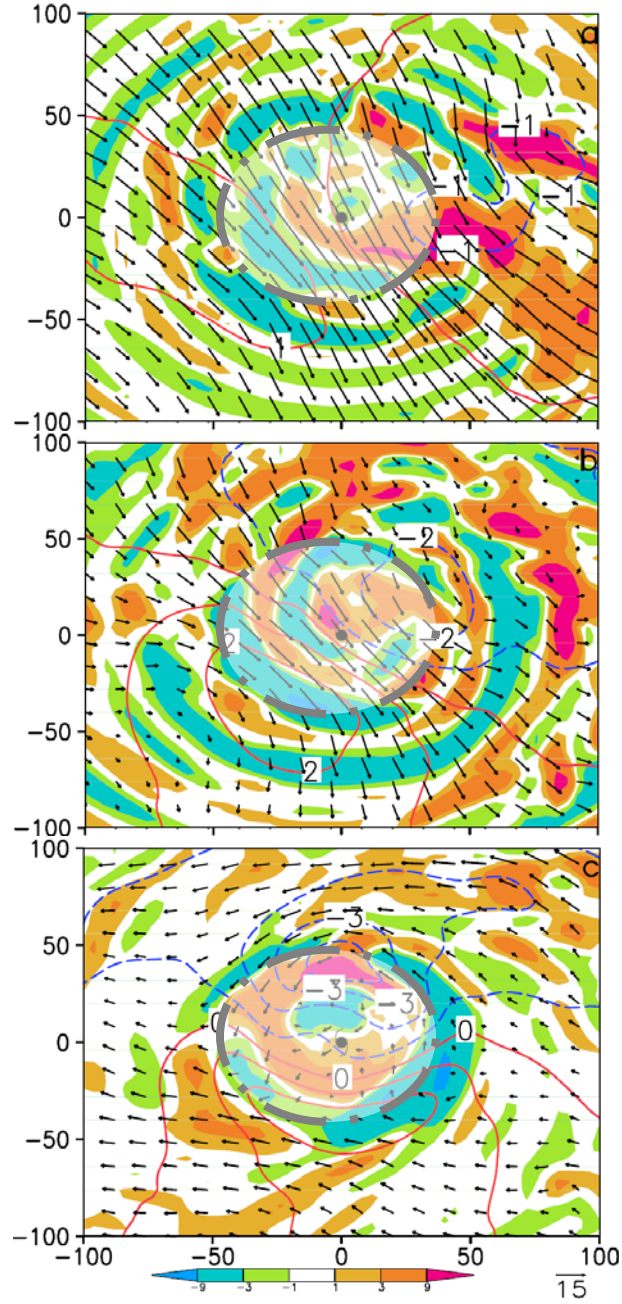


Figure. A15. The sum of pressure perturbations (contoured at intervals of 1 hPa) associated with pieces P1, P2, P3, P4 valid at 0245 UTC 24 August 1998 of Hurricane Bonnie for (a) $z = 10$ km, (b) $z = 5$ km, and (c) $z = 1$ km. All are superimposed by the wind field induced by the all PV anomalies. Shadings denote the total PV anomaly. Solid (dash) lines are for positive (negative) values

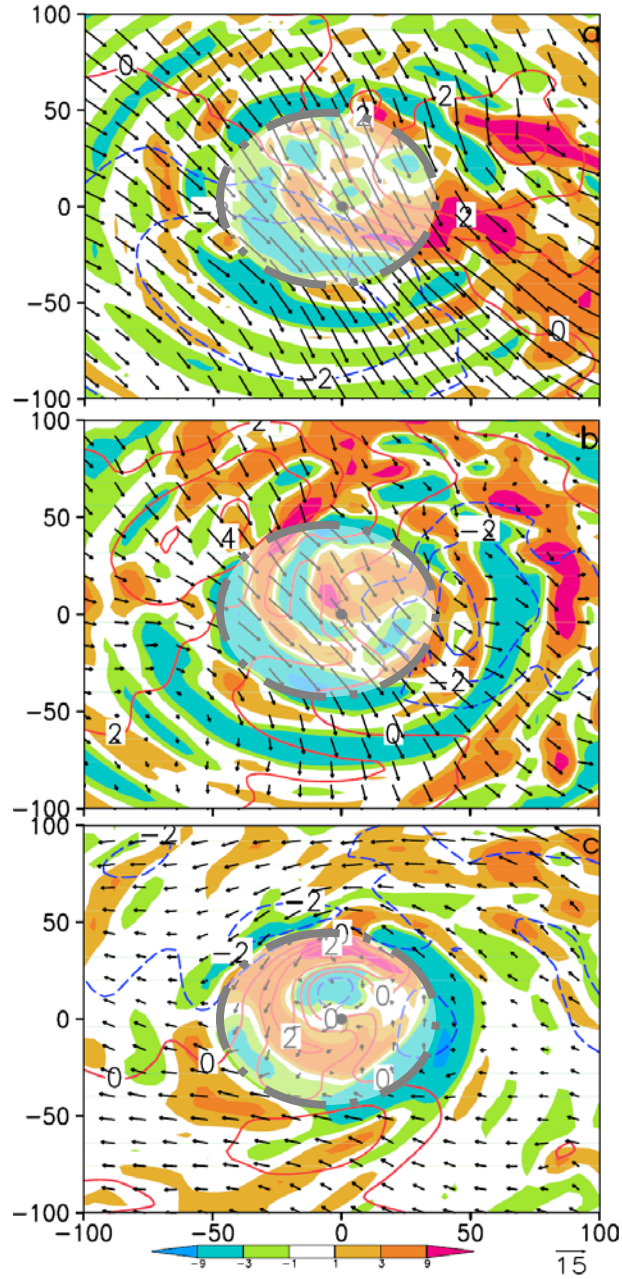


Figure. A16. The sum of potential temperature perturbations (contoured at intervals of 1 K) associated with pieces P1, P2, P3, P4 for (a) $z = 1$ km, (b) $z = 5$ km, and (c) $z = 10$ km. Solid (dash) lines are for positive (negative) values